Assessing volumetric change distributions and scaling relations of retrogressive thaw slumps across the Arctic

Philipp Bernhard[1], Simon Zwieback[2], Nora Bergner[1], and Irena Hajnsek[1,3]

[1]Institute of Environmental Engineering, ETH Zurich, 8093 Zurich, Switzerland ETH Zürich
[2]Geophysical Institute, University of Alaska Fairbanks, Fairbanks, AK 99775 USA
[3]Microwaves and Radar Institute, German Aerospace Center (DLR) e.V., 82234 Wessling, Germany

Correspondence: Philipp Bernhard (bernhard@ifu.baug.ethz.ch)

Abstract. Arctic ice-rich permafrost is becoming increasingly vulnerable to terrain altering thermokarst, and among the most rapid and dramatic of these changes are retrogressive thaw slumps (RTS). They initiate when ice-rich soils are exposed and thaw, leading to the formation of a steep headwall which retreats during the summer months. The impacts and the distribution and scaling laws governing RTS changes within and between regions are unknown. Using TanDEM-X-derived digital elevation models, we estimated RTS volume and area changes over a 5-year period and use probability density functions to describe their distributions. ~~We contrasted 10 study sites (Eurasia: 5, North America: 5), with a total size of 220 000 km^3.~~ Over ~~the 5 year~~ time-period all 1853 RTSs ~~combined~~ mobilized a ~~total~~ volume of $17 \cdot 10^6\,\mathrm{m}^3\,\mathrm{yr}^{-1}$ corresponding to a volumetric change density of $77\,\mathrm{m}^3\,\mathrm{yr}^{-1}\,\mathrm{km}^{-2}$. Our remote sensing data revealed inter-regional differences in mobilized volumes, scaling laws and terrain controls. The distributions of RTS area and volumetric change rates followed an inverse gamma function with a distinct peak and an exponential decrease for the largest RTSs. We found that the distributions in the high Arctic were shifted towards larger values. The area-to-volume scaling ~~could be~~ well described by a power law with an exponent of 1.15 across all study sites, however the individual sites had scaling exponents ranging from 1.05 to 1.37, indicating that regional characteristics need to be taken into account when estimating RTS volumetric changes from area changes. Among the terrain controls on RTS distributions that we examined, slope, adjacency to waterbodies and aspect, the latter showed the greatest, but regionally variable association with ~~thaw slump~~ occurrence. Accounting for the observed regional differences in volumetric change distributions, scaling relations and terrain controls may enhance the modelling and monitoring of Arctic carbon, nutrient and sediment cycles.

1 Introduction

About 15 % of the landmass in the northern Hemisphere is underlain by permafrost (Obu, 2021). With climate warming these permafrost regions become increasingly vulnerable to thaw. This thaw manifest itself first in a slow but gradual deepening of the seasonally thawed active layer (press disturbances) and secondly in a more rapid and local way by the development of thermokarst features (pules disturbances) (Grosse et al., 2011; Schuur et al., 2015). Both forms of permafrost degradation have major impacts by changing ecosystem and hydrological equilibria and impact the Earth system on a global scale by reinforcing climate change with the additional mobilization of organic carbon that was previously stored in the frozen soil. One important thermokarst feature arising from pulse disturbances are retrogressive thaw slumps (RTS). These RTSs initiate by the exposure of ice-rich soils with a subsequent thaw and the formation of a steep headwall (Burn and Lewkowicz, 1990; Kokelj et al., 2009). During the summer, the ice in the headwall melts which leads to a continuous retreat. This process can mobilizes vast quantities of sediments on time scales of years. In the context of recent climate warming an increase in the number and sizes of RTSs in permafrost regions has been found (Lantz and Kokelj, 2008; Lantuit and Pollard, 2008; Gooseff et al., 2009; Kokelj et al., 2009; Lewkowicz and Way, 2019). However, the inter-regional differences in the rates of thaw slumping in terms of their magnitude, distribution and controls remain poorly constrained and so are the implications for carbon and nutrient cycles.

For the investigation of landslides in temperate climate zones, frequency distributions and scaling laws of various form have been used to quantify hazards and ecosystem impacts as well as to improve the process understanding of landslide activity (Tebbens, 2020). The variability and similarities of these laws in terms of landslides properties and area characteristics have played an important role. The soil properties (ice-content) as well as timescales (single event vs. polycyclic multi-year retreat) are different for RTSs than other landslides, but nevertheless the methods used as well as the universality of landslides characteristics could provide valuable insights into RTS drivers and controls. Furthermore, due to the strong spatial variability of soil-carbon densities as well as RTS activity past model estimates of the impacts of RTSs on the carbon cycle have large uncertainties (Turetsky et al., 2020). ~~Currently there is only one study quantifying the area frequency distributions of RTSs, were orthophotos for a study site on Svalbard was used to measure the area disturbed by RTSs (Nicu et al., 2021).~~ Quantifying the RTS frequency distributions and scaling laws as well as their variability across regions have the potential to greatly improve future carbon release rates.

Two of the most common methods to describe landslides are the frequency distribution as well as the area-to-volume scaling. For the frequency distribution the area (or volume) change of the erosion site showing elevation loss is used. In this distribution typically two parts can be distinguished, an exponential decay part describing larger landslides and a deviation from this power-law for smaller events with a distinct peak, indicating the most common landslides in the region. The exponential decay part is well explained by models that merge closely proximal landslides. The attribution of the deviation from the power law is more controversial and is either attributed to an under-sampling of small events or to real physical processes (Tanyaş et al., 2018). The second scaling law, namely the area-to-volume scaling, is based on an observational relation between landslide area and volumetric change. Many studies of landslides inventories that include different sizes, slope failure mechanisms and locations show that area-to-volume scaling follows a power law relation $V \propto A^{\alpha}$ with α ranging from 1 to 1.5. (Larsen et al., 2010).

In a pure mathematical sense, an α of 1.5 corresponds to a situation where objects scale in an invariant way, meaning that if the height dimension is increased by a certain amount, the horizontal (area) dimension is increased by the same. Consequently a scaling coefficient smaller than 1.5 corresponds to a situation where an increase in area leads to a smaller but proportional increase in height (Klar et al., 2011). The ability to estimate the volumetric change from area measurements can especially be useful for estimating the amount of mobilized material if only area measurement are available. Additionally, differences in α between regions may suggest different physical drivers of RTS development.

To quantify these relations for RTSs, remote sensing techniques are the most feasible due to the remote landscape and the severe climate conditions. Digital elevation models (DEMs) that cover the pan-Arctic permafrost terrain with a high enough resolution to study RTSs only became available in the last few years. One of these high resolution DEMs is based on single-pass interferometric ~~SAR~~ observations taken by the TanDEM-X satellites. TanDEM-X is a high-resolution single-pass interferometry satellite mission that was launched by the German Aerospace Center (DLR) with the purpose of generating a high resolution global DEM (Krieger et al., 2007). The satellite pair started observations in 2010 and have observed the global land mass two to three times, now. The expected spatial resolution of about 10 to $12\,\mathrm{m}$ and vertical height resolutions of the order of about 2 to $3\,\mathrm{m}$ is smaller than typical RTS change rates and can thus provide accurate estimates of the thaw slump topography as well as related controls on RTS processes like aspect, slope, and location (Bernhard et al., 2020).

In this study we use DEMs generated from TanDEM-X observations to derive the volume and area change rates of RTSs of several Arctic regions. Additionally we derive several terrain controls namely the aspect, slope, and location. This work focuses on answering the following questions:

1. Does the area and volume change probability density function of RTSs follow the typical landslide distribution and to what extent does the function vary across the study sites?
2. What are the area-to-volume scaling law coefficients for the study sites and are they different?
3. Do the terrain controls vary between the study sites, and if so is the variation related to RTS size?

The large number of RTSs in our sample and the diverse nature of our study sites allow for a robust statistical inference in answering these questions. The results should provide valuable insights concerning susceptibility modelling and will further improve our understanding of the process that govern RTS initiation and growth as well as their future impacts on ecological and hydrological systems.

2 Study Sites

We chose 10 different study sites located in permafrost regions across the Arctic (Figure 1). The selection was first based on sites where previous studies have shown RTS activity: the Peel Plateau and Richardson Mountains ("Peel"), Banks Island ("Banks"), the western Mackenzie River Delta uplands and Tuktoyaktuk Coastlands ("Tuktoyaktuk") and Ellesmere Island ("Ellesmere") that are all located in northern Canada, the Noatak Basin ("Noatak") in Alaska, and the Yamal and Gydan Peninsula in Siberia (Lacelle et al., 2010; Balser et al., 2014; Segal et al., 2016; Nitze et al., 2017; Jones et al., 2019; Nesterova

et al., 2019). Additionally, we chose three study sites in Siberia that exhibit RTS activity but are not well studied, namely on the Taymyr Peninsula ("Taymyr 1 and 2") and on the Chukotka Peninsula ("Chukotka").

The study sites are located in the Arctic tundra and the boreal-tundra transition regions within the continuous permafrost zone (Brown et al., 2002). ~~They show differences in~~ environmental properties including permafrost type, topography, lake-abundance, and vegetation type. ~~Within these extensive regions~~ we selected representative locations for our study sites. The exact outline of the study sites were based on the Sentinel-2 tiling to facilitate the data processing steps.

The amount of ground ice on a pan-~~arctic~~ scale has not been well characterized, but estimations on coarse scale report ground ice contents of $>10\%$ for all study sites (Brown et al., 2002). On large scales, high ground ice content is associated with the climatic history (e.g. syngenetic ice-wedges) and the associated extent of past glacial ice (e.g. buried glacial ice). On small scales ground ice content can vary due to for example soil type (Lacelle et al., 2004).

The study sites on Peel, Banks, Ellesmere, Noatak and Chukotka show strong variation in topography with elevation changes of several hundred meters inside the study sites. The remaining sites show only small variation in elevation (<100m). Another difference between the study sites is in the amount of lakes present. The study site with the most abundance of lakes are in Tuktoyaktuk and Taymyr 2. Only small amounts of lakes are found on Ellesmere and in Noatak (Table 1).

Figure 1. Overview of the study sites. The study sites are distributed around the Arctic with four study sites in northern Canada, one located in Alaska and five in Siberia. The purple area shows the zone of continuous permafrost (Brown et al., 2002).

Table 1. Overview of study sites with size, lake area percentage, elevation range, and number of processed TanDEM-X observations.

Study sites	Size [$10^3 \mathrm{km}^2$]	Lake area [%]	Elevation [m]	TanDEM-X obs. [N]
Peel	19.3	4.3	100 - 1500	307
Banks	6.6	6.3	0 - 400	62
Tuktoyaktuk	7.7	14.7	<100	87
Ellesmere	9.5	2.2	0 - 650	164
Noatak	16.3	1.5	400 - 1400	134
Yamal	24.8	6.0	<100	143
Gydan	14.6	8.9	<100	87
Taymyr 1	23.6	4.1	<100	128
Taymyr 2	11.0	11.1	<100	124
Chukotka	87.9	1.4	0 - 1100	262

Note: ~~The lake area percentage was calculated using the generated waterbody mask. Open waterbodies were not included in the calculation.~~

3 Methods

3.1 Data and Processing

For the DEM generation we used TanDEM-X observations acquired between 2010 and 2017. To ensure adequate vertical accuracies, we only used acquisitions with a height of ambiguity smaller than 80 m (Martone et al., 2012). The radar incidence angles range from $36°$to $44°$. For an accurate orthorectification we used the TanDEM-X 12m DEM as reference and iteratively updated the look-up table based on the measured deviation (Leinss and Bernhard, 2021). We only studied winter acquisitions, because ~~outside the winter months thawed~~ vegetation, wet snow and standing water induce sizeable errors (Bernhard et al., 2020), whereas in winter we expect the low average monthly temperature to produce a dry snow-pack ~~and~~ radar waves can propagate ~~through~~ to the ground without being strongly affected (Millan et al., 2015; Leinss and Bernhard, 2021). ~~For the DEM generation we followed a standard approach~~ (Fritz et al., 2011)~~. The resulting DEMs~~ have a planimetric resolution of about 10 to $12\,\mathrm{m}$ and vertical accuracies of about $2\,\mathrm{m}$ in areas with high coherences. The interferometric processing was done using the *Gamma Remote Sensing* software (Werner et al., 2000). More processing details including tilt-removal and correction of misalignments, specifically for DEMs generated from ~~interferometric SAR~~ observations in permafrost regions can be found in Bernhard et al. (2020).

3.2 RTS detection and manual mapping of affected areas

DEMs corresponding to the same winter were averaged and mosaicked. We then used an automated detection algorithm to identify significant elevation changes in the DEM difference images from DEMs that were obtained more than 3 years apart (Bernhard et al., 2020). For each detection several processing steps were carried out. First the topography and environment were assessed using a TanDEM-X DEM and Sentinel-2 multispectral images taken in summer (snow-free). For all study sites at least one Sentinel-2 image during the years 2016 to 2019 was available. The criteria for classifying a detection as an active RTS were the exposure of bare soils, a retreat over time, a location related to a potential sediment removal mechanism, and the presence of a headwall (Lantuit and Pollard, 2008; Nitze et al., 2018; Lewkowicz and Way, 2019). In uncertain cases additional time-series of Planet Rapid-Eye optical data was used to classify the detections (Planet-Team, 2018).

The error sources and uncertainties that govern the lower RTS detection limit in terms of headwall height and retreat rate are manifold and difficult to quantify~~.~~ This is mainly due to the small amount of available high resolution, three dimensional RTS inventories (Swanson and Nolan, 2018; Van der Sluijs et al., 2018), ~~were also~~ time-scale~~s~~ on which the RTSs are monitored plays an important role. To get an estimate on the lower limit of RTS induced elevation changes ~~to be~~ detectable we ~~can~~ analyse the smallest detected RTSs in our sample. The 10 smallest detected RTSs have elevation changes in the range of 1.6 to $1.9\,\mathrm{m}$ ~~and can be seen as an approximation for the smallest RTS headwall heights that are detectable, which are on the same order then the general TanDEM-X DEM accuracies~~. Similarly, the smallest total area changes of detected RTSs are on the order of 500 to $1000\,\mathrm{m}^2$, corresponding to about 10 to 12 pixels. Consequently, if the size of the erosion feature~~s~~ approaches the pixel resolution ~~also~~ the accuracy of the estimated volume loss increases. Additionally, processes related to the observation properties and interferometric processing further complicate the error estimations. For example the ~~about~~ 40 degree right-looking viewing

geometry leads to different pixels resolution depending on aspect and slope of the observed area. These error sources and increased uncertainties ~~especially for small RTSs, both in terms of spatial and vertical changes,~~ should be considered in the interpretation and future use of the dataset.

After the classification step we generated polygons for each detected RTS outlining the area with significant elevation change. Examples of the generated polygons are shown in the Supplement (Figures S1 to S4). The polygons outlining the area of elevation change were drawn by a trained student and the first author, as our use of an automated method that implemented a fixed threshold on the elevation change gave unreliable results. The RTS polygons were attributed in terms of location as either "shoreline" (located close to a waterbody) or "hillslope" (located at trenches or riverbeds).

3.3 RTS attributes

For all calculations we used the polygon, which indicate an area of elevation change and thus a net volume loss. We note that this area can also include a zone of deposition, especially for small and low-relief RTSs or if the time between observations increases. We could not accurately detect areas such as the debris tongues or zones of alluvial deposits and they are not included. We computed the volumetric and area change as well as the slope and aspect. For parts of the study sites observations during winters in 2010/11, 2011/12 and/or 2012/13 were available. To simplify the analysis we normalized the properties to changes per year and took the average if several DEM difference pairs were available. It is important to note that unlike most landslides, RTSs are multi-year features with a strong variability in the erosional intensity as well as a potential change of their morphology over time. In the interpretation of the results and specifically the comparison to landslide studies, the use of the integrated change over several years needs to be considered. We computed the aspect and slope by using the pre-disturbed elevation model and applied gaussian smoothing with a standard deviation corresponding to 100 m to reduce the influence of random errors (Kang-tsung and Bor-wen, 1991). For the aspect distribution we additionally computed the aspect distribution weighted by volume.

To quantify the volumetric change rate density (volumetric change rate per unit area) we first use a simple approach by dividing the summed total of all RTS volumetric changes per year by the study site size. This has a drawback because RTSs often occur heterogeneously and the result strongly depends on the exact outline of the study sites (Ramage et al., 2017). For example, in the Peel study site only the east facing part of the mountain range experiences RTS development, but our study site also includes the western part of the range where nearly no RTS activity was detected. To account for this problem we follow a similar approach than proposed in Kokelj et al. (2017) and divide our study site into tiles of sizes 10 km by 10 km and counted the number of empty grid cells and computed a more representative RTS density using only the cells showing RTS activity. It is to note that to interpret the computed density values the number of empty as well as the number of non-empty grid cells in relation to the total size of the study site should be considered.

To quantify the amount of lakes in each study site we used the waterbody mask generated from Sentinel-2 data and computed the area that is covered by the mask (McFeeters, 1996; Kaplan and Avdan, 2017). For this computation, we excluded open sea areas.

We investigated the dependency of RTS growth on different terrain controls by computing the aspect, slope, and location

(lakeshore or hillslope). For the aspect we identified the most dominant orientation by summing the number of RTSs as well as the volumetric and area change rates in 8 aspect bins (N, NE, E, SE, S, SW, W, NW) and used these bins to compute the strength and orientation of the primary direction.

3.4 Change Rate Distributions

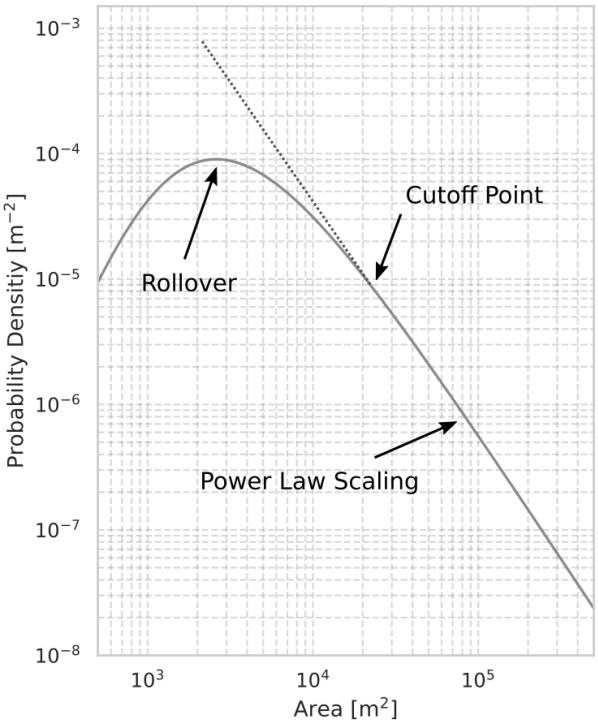

Figure 2. Schematic representation of RTS area probability density function. Two parts can be distinguished: An exponential decay part above the cutoff value and a deviation from the power-law scaling below the cutoff point.

The probability density function (PDF) of the area affected by elevation loss per year corresponding to an RTS inventory can be defined as

$$\mathrm{p}(\mathrm{A_{RTS}}) = \frac{1}{\mathrm{N_{RTS}}} \frac{\delta \mathrm{N_{RTS}}}{\delta \mathrm{A_{RTS}}} \tag{1}$$

where $\mathrm{A_{RTS}}$ is the area change affected by elevation loss of a RTS per year, $\mathrm{N_{RTS}}$ the total number of RTS in the inventory, $\delta \mathrm{N_{RTS}}$ the number of RTS with affected areas between $\mathrm{A_{RTS}}$ and $\mathrm{A_{RTS}} + \delta A_{RTS}$ and $\delta \mathrm{A_{RTS}}$ is the bin width. Equivalently the probability density function $\mathrm{p}(\mathrm{V_{RTS}})$ for the volumetric change per year can be defined.

All RTSs in the study show changes per year in the range of 10^2 to 10^6 $\mathrm{m^2\ yr^{-1}}$ for the area and 10^2 to 10^6 $\mathrm{m^3\ yr^{-1}}$ for the volume, and we used 30 bins sampled in log-space to cover these ranges.

When analysing a landslides PDF three quantities can be used to describe the distribution: the rollover- and cutoff-points for small events and the coefficient of the power law scaling β for large events. The rollover point is defined as the peak in the PDF and corresponds to the most common occurrence in the distribution. For large RTSs the PDF can be described as a power law function. The point at which the distribution starts to follow a power law is defined as the cutoff point (Figure 2).

To determine how well the data points are described by this model and to estimate the rollover point we fitted a three parameter Inverse Gamma Function to the RTS probability density function (Malamud et al., 2004). To estimate the error of the fit we used the bootstrap method drawing 1000 random samples with replacement from all data points, and computed the R^2 value as well as the rollover point for each iteration (Ohtani, 2000).

For the computation of the cutoff value and the exponential scaling exponent we used the method of Clauset et al. (2009) which is commonly used in landslide frequency-area analyses (Bennett et al., 2012; Parker et al., 2015; Tanyaş et al., 2018). The approach is based on sampling all possible cutoff values and estimating the corresponding exponential scaling coefficients β using a maximum-likelihood fitting method. The obtained fitting values are then tested based on a Kolmogorov-Smirnov statistic and the values that follows best a true power law distribution are used as the final cutoff and β value. To quantify the uncertainty we again used a bootstrap algorithm.

3.5 Area-Volume scaling

One important quantity in comparing landslides of various sizes is the change relation between area and volume. The simplest conversion assumes that an anisotropic scaling exponent α, ~~which~~ relates the area and volume by: $\mathrm{V} \approx \mathrm{A}^{\alpha}$. Since both variables (area and volume) are affected by measurement errors we used an orthogonal distance regression model to fit a straight line (Boggs and Rogers, 1990; Markovsky and Van Huffel, 2007). To quantify the goodness of the fit we calculated the RMSE, R^2 and p-value (in log-space).

4 Results

We investigated 10 different study sites and measured the area and volumetric change rates of 1854 RTSs over a 4 to 5 year time-frame. Due to the low density of RTSs in Yamal and Gydan and the two study sites in Taymyr we combined these to one study site (in the following "Yamal/Gydan" and "Taymyr") according to their geographical and geophysical proximity.

The number of RTSs per study site and the obtained volumetric change rates in terms of the total volume, density, and changes per RTS are shown in Table 2. We found the largest RTSs in terms of average volumetric change rates per RTS at Ellesmere, Peel, and Banks with yearly average change rates of $13\,200\,\mathrm{m}^3\ \mathrm{yr}^{-1}$, $12\,200\,\mathrm{m}^3\ \mathrm{yr}^{-1}$, and $10\,700\,\mathrm{m}^3\ \mathrm{yr}^{-1}$. The other areas show much smaller yearly average volumetric change rates in the the range of $2\,400\,\mathrm{m}^3\ \mathrm{yr}^{-1}$ (Tuktoyaktuk) to $3\,600\,\mathrm{m}^3\ \mathrm{yr}^{-1}$ (Taymyr). Compared to the other study sites, RTSs at Ellesmere, Peel, and Banks also show higher volumetric change both in terms of overall change per study site size (density) as well as per individual RTS. Furthermore, these three sites also contain the largest overall size RTSs of the investigated study sites (Figure 3).

In the following paragraphs we will present (1) a characterisation of the area and volumetric changes rates with special em-

phasis on the probability density functions with the estimation of the rollover, cutoff and exponential decay components; (2) the estimated area-to-volume scaling laws; and (3) several terrain controls that could potentially be related to RTS size and frequency. To compare the quantities estimated in ~~these~~ three sections we computed the correlation coefficients between them.

Table 2. Number of RTSs in each study site with the total number of RTS and the volumetric change rates in terms of total change, density and average rates per RTS.

Area	N_{RTS} [N]	V_{change}^{total} [$10^6 m^3\ yr^{-1}$]	V_{change}^{mean} (density) [$m^3\ yr^{-1}\ km^{-2}$]	V_{change}^{mean} (RTS) [$10^3 m^3\ yr^{-1}\ RTS^{-1}$]
Peel	438	5.27	342.8	12.2
Banks	679	7.16	883.8	10.7
Ellesmere	223	2.95	546.7	13.2
Tuktoyaktuk	212	0.5	43.3	2.4
Noatak	26	0.09	14.9	3.4
Yamal/Gydan	128	0.37	12.4	2.9
Taymyr	97	0.35	11.3	3.7
Chukotka peninsula	51	0.17	3.8	3.5

4.1 RTS volume and area distributions

The estimated PDFs are shown in Figure 4a and 4b. For most areas the quality of fit of the inverse gamma function was good, as indicated by R^2 values > 0.75. Exceptions were the Noatak and Chukotka study sites with R^2 values between 0.6 and 0.7. These two sites also have the lowest number of RTSs in the sample with only 26 (Notatak) and 51 (Chuktoka) RTSs (Figure 4c and 4d).

The modes of the volume change distributions (rollover points) differ between sites. The two study sites located in the high Arctic (Ellesmere and Banks) show an order of magnitude higher rollover values. The range of measured volumetric and area change rates show large variations for the Tuktoyaktuk and Peel study sites, whereas the other study sites show smaller variations.

The PDFs above the cutoff value, the relation between rollover and cutoff as well as the exponential decay values differ between sites (Figure 5). For the PDF based on the volumetric change, a high rollover value is moderately associated with high cutoff values indicated by a correlation coefficient of 0.72. By contrast, the PDF based on the area change rate shows a much stronger separation between the high Arctic sites and the other study sites and consequently also shows a high correlation factor of 0.96. For the power law exponent for RTSs above the cutoff values no large difference between the areas is visible ($\beta \approx 2$ to 3 and correlation coefficients < 0.64). All correlation coefficients are shown in the Supplement (Figure S5). It is to note that for the yearly area and volumetric change rates the cutoff value for the Peel study site is relatively small but the distribution continues to high values with yearly area change rates of up to $6 \cdot 10^4 m^2 yr^{-1}$ and $3 \cdot 10^5 m^3 yr^{-1}$ (Mega-Slumps). The computed values

of the rollover, cutoff, and exponential decay coefficients as well as the fit parameters for the inverse gamma function are reported in the Supplement Tables S1 and S2.

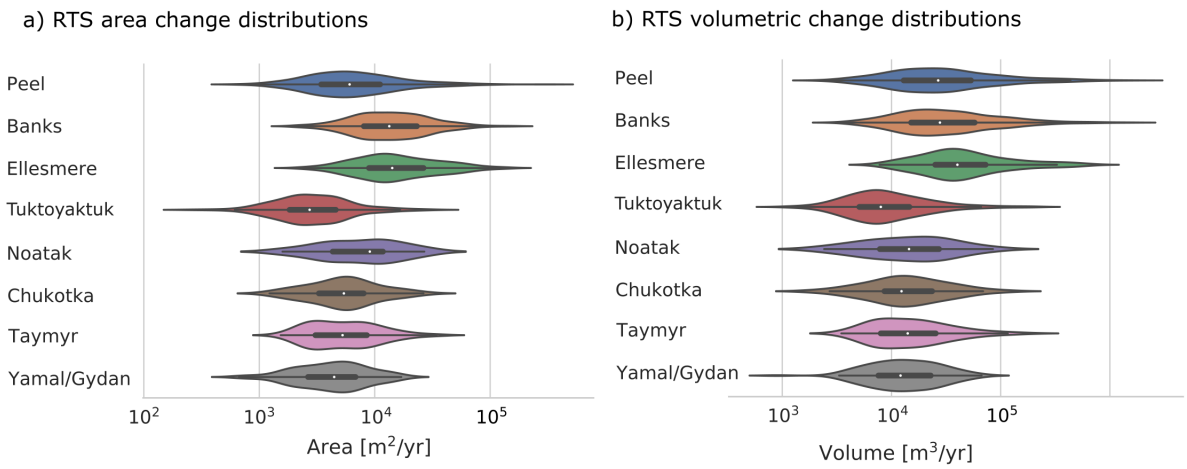

Figure 3. Area a) and volumetric b) change rate distributions of mapped RTSs in form of violin plots. The white dots on the center lines indicate mean values for the set of study sites. For each violin plot the white dot on the center line indicates the mean value, the thick center line shows the interquartile range, the thin center line shows the total range of data, and the colored area indicates the probability density of the data across the distribution of values smoothed by a kernel density estimator.

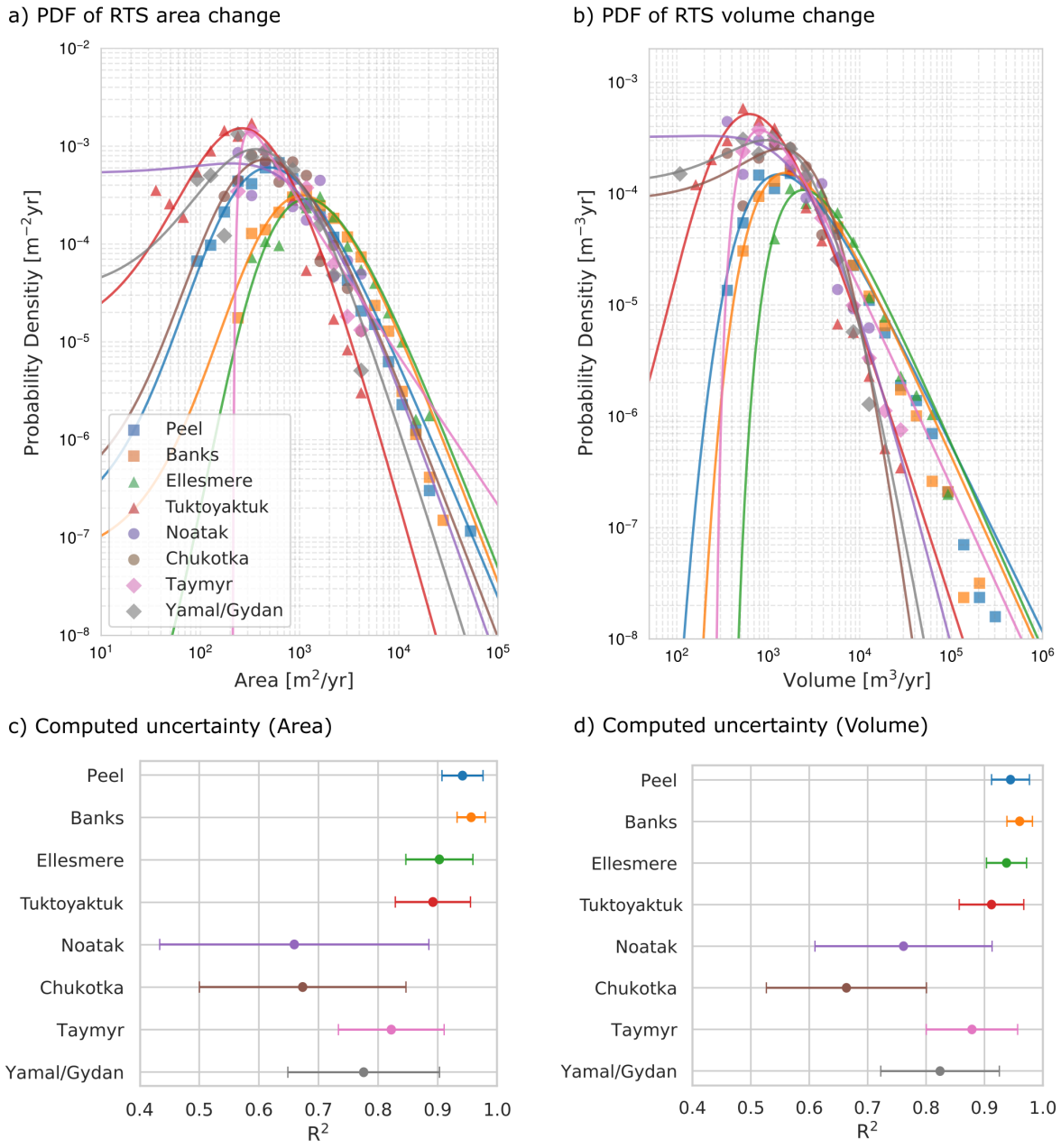

Figure 4. PDF of area and volumetric change rates of mapped RTSs for the set of study sites. a) and b) show the PDFs of area and volumetric change rates with fitted inverse gamma functions. c) and d) show the computed R^2 errors.

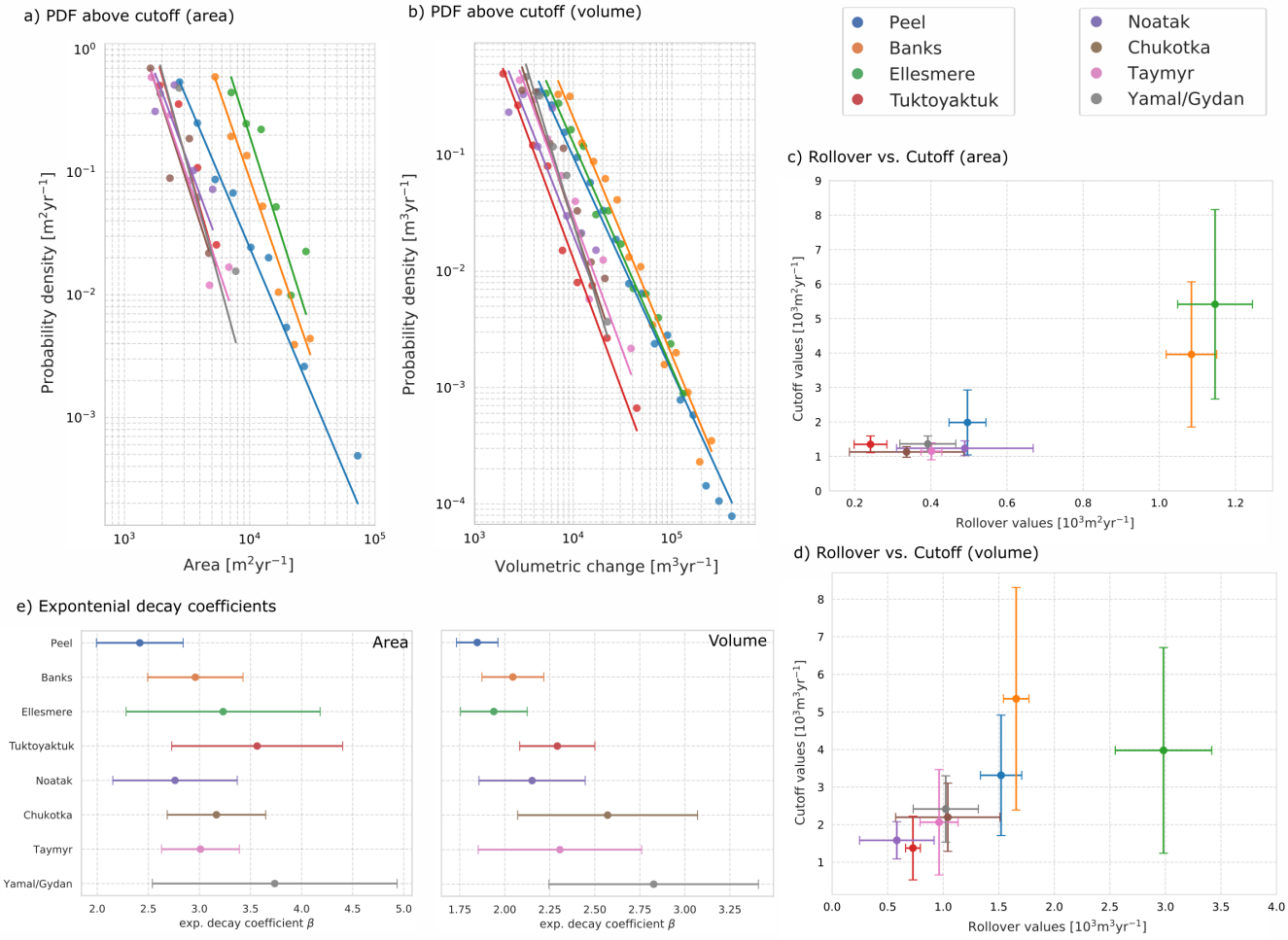

Figure 5. Cutoff, rollover, and exponential decay coefficents. a) and b) shows the PDFs for yearly area and volumetric change rates above the cut-off values. c) and d) shows the estimated rollover and cutoff values for yearly area and volumetric change rates. e) Exponential decay coefficients for fits above the cutoff.

4.2 Area-to-volume scaling

The estimated area-to-volume scaling law based on all data points in log-log space shows a clear relationship that spans over four orders of magnitude between the area and volumetric change rates (Figure 6a). The estimated scaling exponent across all study sites was $\alpha = 1.15 \pm 0.01$. The quality of fit was decent, with a R^2 value of 0.81, RMSE of 0.21 $m^3 yr^{-1}$ and p-value smaller than 10^{-6} showing a strong dependency between RTS area and volumetric change rates. This is remarkable considering that RTSs in the sample occurred in different topographic and geomorphological settings. Nevertheless we found a moderate inter-region variability in the scaling coefficient. The α coefficients for the individual sites was in the range of 1.05 to 1.25 with the exception of RTSs in the Banks site with a high coefficient of 1.37 (Figure 6b). The data points and fitted lines for each study site individually can be seen in the Supplement Figure S6. The strong association between area and volume change rates can facilitate the estimation of volume changes from multispectral satellite images.

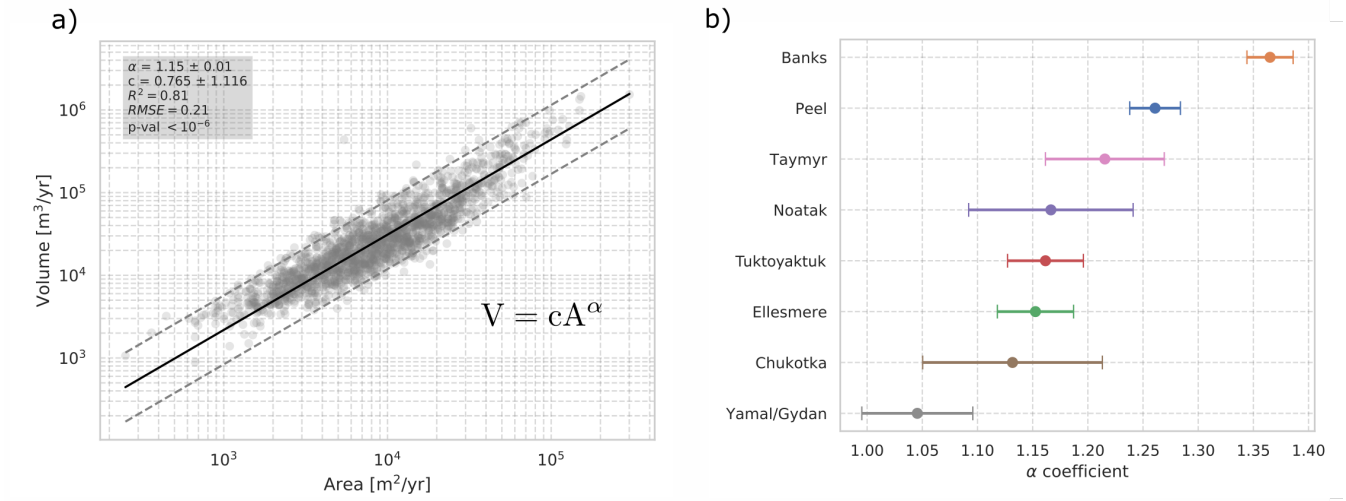

Figure 6. Area-to-volume scaling laws for RTS in the set of study sites. a) shows the total dataset with all study sites combined. We found an exponential scaling exponent of $\alpha = 1.15 \pm 0.01$. b) shows the computed values of the scaling exponent for each site individually with the estimated standard deviation. A large variation between 1.05 and 1.37 is visible.

4.3 Terrain controls

Among the investigated terrain controls, aspect shows the greatest variability between the study sites. RTSs located in Siberia as well as on Ellemere tend to favour a South-West facing orientation (Figure 7a). The very small number of RTSs in the Noatak study site showed a preferred orientation towards the North-West and RTSs in Peel have a preferred orientation towards the North-East. For Tuktoyaktuk and Banks no clear trend is visible. To consider the possibility of more than one preferred orientation we additionally looked at the initial aspect bin distribution (Supplement Figure S7). Here only the aspect distribution of RTSs in the Noatak valley shows two preferred orientation, but this could be related to the low number of RTSs in the study site. Additionally to the number of RTSs in each aspect bin we weighted the aspect by the volumetric change rates. This does only slightly alter the preferred orientation and large RTSs do not occur at different aspects.

The slope of the pre-disturbed area shows some difference between the study sites (Figure 7c). In general all RTSs evolve at slopes ranging from 2° to 3° up to slopes of 20°. Interestingly, in the study site of the largest RTSs on Banks, they tend to favour lower slopes with values below 12° .

We investigated the dependency of RTSs locations in terms of their occurrence. We distinguished two types of locations, either at a shore (including lake and coastal) or at hillslopes with no large waterbodies close by. Several study sites have mostly one type of RTS location. The RTSs in Ellesmere (99% hillslope), Peel (96% hillslope) and Noatak (88% hillslope) have mostly RTSs at hillslope locations. On the contrary, RTSs in the Tuktoyaktuk site are nearly all located at lakeshores (99%). All other study sites have a mixture of hillslope and shoreline RTS locations: Banks (66% hillslope), Chukotka (52% hillslope), Taymyr (27% hillslope) and Yamal/Gydan (26% hillslope). In the study sites with both types of RTS locations no significant difference between the distributions is visible (Figure 7c). Furthermore, we did not find a significant correlation between RTS size and the percentage of hillslope or shoreline RTS locations (Supplement Figure S5).

To estimate the volumetric change rate density of RTSs within the RTS-affected regions of each study site we gridded them into tiles of size $10\,\mathrm{km}$ by $10\,\mathrm{km}$. Figure 8a shows the volumetric change rates per square kilometre using only the tiles with RTSs present. The volumetric change densities over the total study site strongly depends on the exact outline of study sites and removing tiles without RTSs present gives a more consistent and comparable volumetric change rate density. To make this more visible the amount of tiles with RTSs present and without can be seen in Figure 8b. Here for example, the Chukotka Pensinsula has only a small number of tiles with RTSs present.

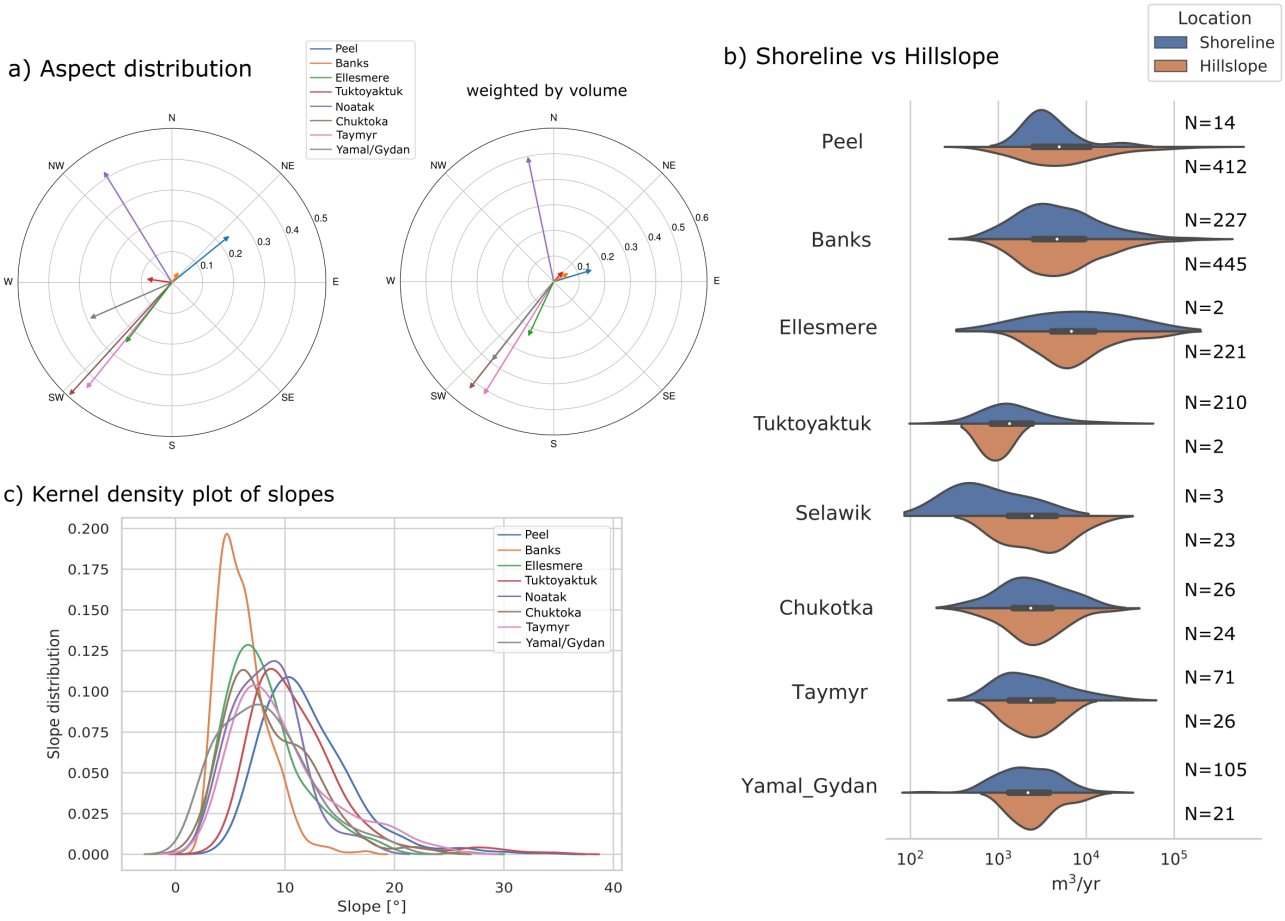

Figure 7. Terrain controls of mapped RTSs for each study site. a) shows the aspect main orientation of RTSs in each study site (left) and additionally weighted by the volumetric change rates (right). b) shows the probability density distributions of volumetric changes rates in form of a violin plot. ~~The top part of each violin indicates the subset of shoreline RTSs and the bottom part the subset of hillslope RTS as probability density of the data across the distribution of values smoothed by a kernel density estimator.~~ For each violin plot the white dot on the center line indicates the mean value of the entire study site dataset with the thick center line showing the interquartile range. The number of RTSs in each subset is listed on the right. Some sites are dominated by one location type. c) shows the distribution of the pre-disturbed DEM slopes at the RTS locations.

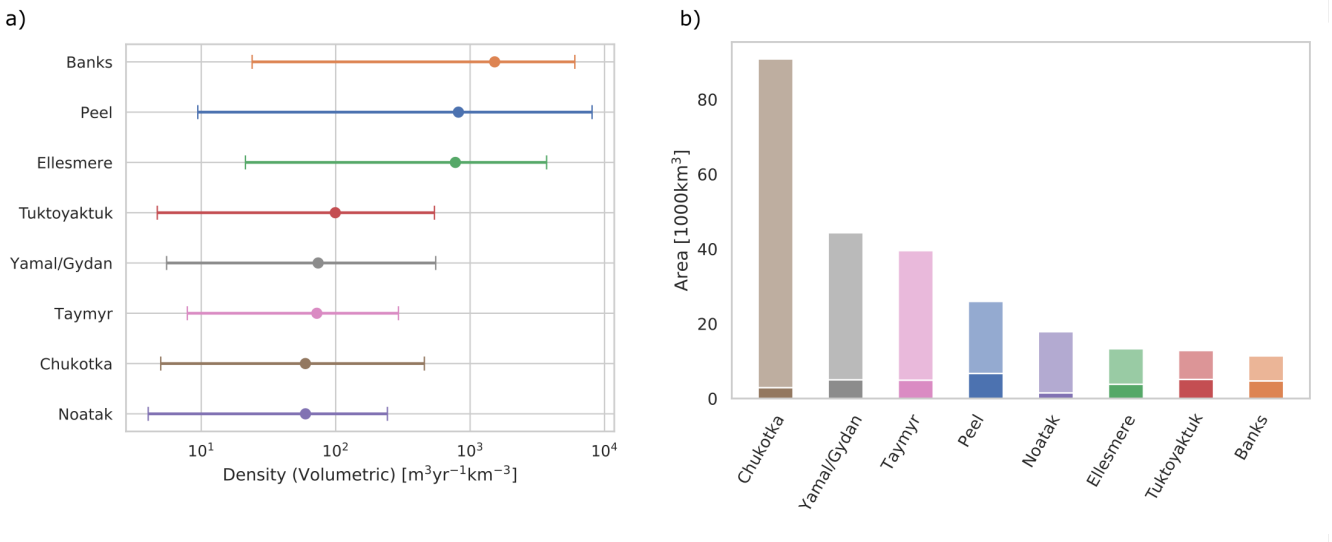

Figure 8. Volumetric change rate densities and density related to study site size for each study site. a) shows the computed RTS volumetric change rate densities using a 10 km by 10 km grid with the empty grid cells removed. The vertical bars indicate the range in the computed densities. ~~(~~b) shows the study site size ~~in transparent~~ with the fraction of tiles with RTS ~~present in~~ solid ~~(b)~~.

5 Discussion

5.1 Probability density functions to characterize thaw slump activity

The computed probability density functions of the yearly area and volumetric change rates follow a characteristic inverse gamma law with first an increase in frequency up to a maximum value with the most abundant thaw slump sizes (rollover) and then a decrease with an exponential decay tail above a certain cutoff value. Our findings show that the applicability of this universal scaling also applies to permafrost landscapes, despite differences in the governing geomorphic processes with respect to lower latitude environments. Here we emphasize again that that another difference between our analyses and that of common landslide studies is that RTSs are a multi-year phenomena with variable yearly erosion rates. Some variability in the exact form of the distributions should therefore be expected if different time periods are chosen.

To further investigate the distributions we distinguish between two parts: (1) the exponential decay part for large RTSs and (2) the part that deviate from this exponential decay below the cutoff point. For landslides the exponential decay part is typically explained in a statistical way by the concept of self-organized criticality, where a constant "input" of a specific landslide size at random location, together with a merger of landslides that are close to each other, reproduces this distribution (Bak and Tang, 1989; Turcotte, 1999). For RTSs this explanation seems plausible since initiation and evolution are strongly linked to soil properties that can promote RTS development in close proximity and also RTS coalescence is common (Lantz and Kokelj, 2008; Lantuit et al., 2012; Wang et al., 2016). In addition to the universal exponential decay behaviour in all study sites we found that the largest RTSs in the Peel, Banks and Ellesmere study sites have order of magnitudes larger growth rates (Figure 5 a,b). A possible explanation is that topographic and geomorphological properties, like the amount of massive ice, overburden thickness or the steepness of terrain only allow RTSs to grow to a certain size (Kokelj et al., 2017; Rudy et al., 2017; Jones et al., 2019). For example in the Tuktoyaktuk study site ($N_{RTS} = 212$) where RTSs occur at lakeshores in mainly flat regions, the largest RTSs show growth rates between $5\,200\,m^2\,yr^{-1}$ and $31\,800\,m^3\,yr^{-1}$ compared to, for example, the Ellesmere site ($N_{RTS} = 223$) with more topographic features and mainly hillslope RTSs which shows 3 to 4 times higher maximum growth rates (range is between $23\,000\,m^2\,yr^{-1}$ and $106\,400\,m^2\,yr^{-1}$). This suggests that additional to the exponential decay factor also a maximum RTS growth rate is important to characterize the high end tail of the probability density function.

For the deviation from the exponential decay, two types of explanation have been proposed for landslides in temperate climate (Tebbens, 2020). First an under-sampling of small landslides due to limitations in resolution and secondly an explanation that attributes this divergence on physical processes. By investigating our dataset a divergence due to under-sampling seems unlikely since the PDFs in Peel, Banks and, Ellesemere show this divergence (cutoff-point) at high yearly change rates of $> 10^4\,m^2\,yr^{-1}$ and $> 3 \cdot 10^4\,m^3\,yr^{-1}$ which corresponds to area and volumetric changes high above the resolution limit (TanDEM-X DEM resolution: Horizontal $\approx 10\,m$, vertical 2 to $5\,m$). The physical origins are likely related to environmental conditions and physical characteristics of ground materials like ground ice-content but are outside the scope of this work. Future models for thaw slump initiation and evolution should be able to investigate the drivers and reproduce such distributions.

5.2 Similarities and differences in Area-Volume scaling

We found a power law relationship ($V \approx A^{\alpha}$) between the area and the volumetric change rates with a scaling coefficients α of 1.15 for the total dataset and ranging between 1.05 and 1.37 for the individual study sites. Such relationship are known from landslides in temperate climates with typically values of 1 to 1.5 (Larsen et al., 2010; Klar et al., 2011). For RTSs only one study by Kokelj et al. (2021), investigating RTSs on the Peel Plateau and Richardson Mountains, has estimated this relationship and found a scaling coefficient of 1.42 which is relatively high compared to our values (Peel: 1.27, Tuktoyaktuk: 1.17) but inside the estimated error.

Comparing the coefficients between study sites we found that lower scaling coefficients are not correlated with smaller RTSs. For example the scaling law coefficient in the Tuktoyaktuk site with relatively small RTSs is the same as for the RTSs in the Ellesmere site with the largest RTSs in our dataset. On the other hand, for RTSs in the Peel study site there is little confining topography and deep layers of ice-rich tills that allow the headwalls to grow to large sizes and consequently yield a steeper regression curve (Lacelle et al., 2015). The diversity in landform characteristics also contributes to the variation of the area to volume scaling coefficient. ~~In~~ the ~~study sites~~ Banks ~~or~~ Noatak, shallow detachments are dominant in the small-area range. These may promote larger scaling coefficients when combined with older, deeper RTSs (Lewkowicz, 1987b). Furthermore, most RTSs initiate as shallow active layer detachments. The gradual increase in headwall heights following the initiation event could lead to a temporal change in the scaling coefficient. Further investigations relating the scaling coefficients to additional RTS and area characteristics (e.g. soil properties, climatic history, age of the RTSs) are needed.

5.3 Terrain controls and their relation to RTS size

With the available data we could determine several terrain controls, namely the orientation of RTS growth, the slope of the predisturbed area the RTS grew into as well as the location in terms of hillslope and shoreline RTSs. Our findings in terms of the preferred orientation of RTSs are mostly consistent with past regional studies: A preferred South-West orientation for RTSs in the Siberian study sites (Nesterova et al., 2019) and Ellesmere (Jones et al., 2019), towards the North-East for the Peel study site (Lacelle et al., 2015) and North facing RTSs in Noatak (Swanson and Nolan, 2018). For RTSs in the Tuktoyaktuk study site we found no preferred orientation consistent with Wang et al. (2009), but in contradiction to other studies that found RTSs orientations that favour North facing slopes (Kokelj et al., 2009; Zwieback et al., 2018, 2020). The association with aspect hints at inter-regional differences in the governing geomorphic drivers and controls. A South-West facing orientation is considered to be related to higher initiation- and growth-rates of RTSs due to the higher energy available from solar radiation (Lewkowicz, 1987a). This would suggest that solar radiation is an important factor in RTS growth and initiation for the study sites in Ellesmere and Siberia. Past studies have shown that a high ground ice content is a necessary condition for RTS development (Kokelj and Jorgenson, 2013; Ramage et al., 2017). During the Holocene Thermal Maximum the regions in North-West Canada experienced warmer summer temperatures than other Arctic regions and could have ~~removed~~ ground ice on South-facing slopes (Burn et al., 1986; Kaufman et al., 2004; Lacelle et al., 2010; Zwieback et al., 2018). Thus the differences in RTS aspect distributions could be related to the climatic history. For example the dominant North-facing exposure on the Peel

Plateau could reflect such anisotropic abundance of ground ice.

We did not find a significant relation between RTS size (area and volumetric change rates) to aspect as well as slope or location (hillslope, shoreline). This finding affirms previous studies that highlighted the complexity of the processes and controls governing RTS expansion.

5.4 Implications

The scaling relations we quantified are critical for modelling and predicting RTS activity and the impacts on biogeochemical cycling. The regional variability in scaling behaviour needs to be considered when upscaling field observations to estimate large-scale nutrient, sediment, and carbon budgets. Because Earth system models strive to capture the variability of these processes from regional to global scales, our results can be used to calibrate and validate global models. Possible changes in the scaling relations could be important indicators to predict future RTS evolution and impacts.

Our observations of variable RTS development rates and regimes highlight the need for continual pan-Arctic monitoring and further satellite missions to derive high resolution DEMs. The TanDEM-X data availability only allowed us to compute elevation changes in a 4 to 5 year time window. To investigate changes in RTS activity related to climate change a higher temporal resolution is needed. Here additional observations from the TanDEM-X satellite as well as data from the ArcticDEM could add additional datapoints (Bachmann et al., 2018; Dai et al., 2020). Furthermore, with the derived area-to-volume scaling laws it is potentially possible to use optical satellite images which are available at a higher temporal resolution to estimate the volumetric change.

6 Conclusions

In this study we quantified the yearly volumetric and area change rates of RTSs over a 4 to 5 year time-frame in 10 study sites across the Arctic with a total study size of 220 000 km^2 and a total number of 1868 RTSs. We found that the frequency distributions of the volumetric and area change rates are well described by an Inverse Gamma distribution ($\mathrm{R}^2 > 0.5$) with the distinct features of a rollover, cutoff and an exponential decay for large RTSs. This kind of behaviour is well known for landslides in temperate climate regions with very different trigger mechanisms and soil properties and could provide valuable insights in modelling future RTS evolution on a pan-Arctic scale.

The comparison between study sites showed that the distribution of RTSs ~~in three study sites~~ in northern Canada (Peel Plateau and Richardson Mountains, Banks Island, Ellesmere Island) are shifted towards higher change rates in volume and area. Nevertheless, the exponential decay rates for large RTSs in all study sites were similar.

Our analyses revealed consistent but regionally variable area-to-volume scaling behaviour. For the total dataset we found a scaling coefficient of $\alpha = 1.15 \pm 0.01$ with some variance between the study sites (α between 1.05 to 1.37).

~~For the aspect~~ ~~we~~ found diverse preferred orientations of RTSs between the study sites from no dominant orientation for Tuktoyaktuk and Banks Island, a North-East orientation for the Peel Plateau and Richardson Mountains, East-facing RTSs in the Noatak Valley and a strong South-West orientation of all study sites in Siberia and the study site on Ellesmere Island.

Our regionally variable RTS scaling relations may be used to constrain large-scale estimates of carbon, sediment and nutrient budgets. By capturing the variability of RTS change rates across scales, remote sensing is a vital tool for predicting hazards and attendant ecosystem changes in a rapidly changing Arctic.

Data availability. Locations and extracted properties of RTSs are available at: https://www.doi.org/10.3929/ethz-b-000482449. The polygons outlining the area of elevation change are available upon request. Sentinel-2 are available from the Copernicus Open Access Hub (https://scihub.copernicus.eu). TanDEM-X CoSSC data are not freely available but can be requested from the German Aerospace Center (DLR) and accessed through the EOWEB (https://eoweb.dlr.de)

Author contributions. PB conducted the DEM processing, analysed the data and drafted the initial manuscript, SZ provided critical guidance and contributed to the writing of the manuscript, NB and PB conducted the manual RTS mapping, IH provided guidance and corrections to the final manuscript.

Competing interests. The authors declare no conflict of interest

References

Bachmann, M., Borla Tridon, D., Martone, M., Sica, F., Buckreuss, S., and Zink, M.: How to update a global DEM - acquisition concepts for TanDEM-X and tandem-L, in: Proceedings of the European Conference on Synthetic Aperture Radar, EUSAR 2018, 2018.

Bak, P. and Tang, C.: Earthquakes as a self-organized critical phenomenon, Journal of Geophysical Research: Solid Earth, 94, 15 635–15 637, 1989.

Balser, A. W., Jones, J. B., and Gens, R.: Timing of retrogressive thaw slump initiation in the Noatak Basin, northwest Alaska, USA, Journal of Geophysical Research: Earth Surface, 119, 1106–1120, https://doi.org/10.1002/2013JF002889, 2014.

Bennett, G., Molnar, P., Eisenbeiss, H., and McArdell, B.: Erosional power in the Swiss Alps: characterization of slope failure in the Illgraben, Earth Surface Processes and Landforms, 37, 1627–1640, https://doi.org/10.1002/esp.3263, 2012.

Bernhard, P., Zwieback, S., Leinss, S., and Hajnsek, I.: Mapping Retrogressive Thaw Slumps Using Single-Pass TanDEM-X Observations, IEEE Journal of Selected Topics in Applied Earth Observations and Remote Sensing, 13, 3263–3280, https://doi.org/10.1109/JSTARS.2020.3000648, 2020.

Boggs, P. T. and Rogers, J. E.: Orthogonal Distance Regression, Statistical analysis of measurement error models and applications: proceedings of the AMS-IMS-SIAM joint summer research conference held June 10-16, 1989, 112, 186, 1990.

Brown, J., Ferrians, O., Heginbottom, J. A., and Melnikov, E.: Circum-Arctic Map of Permafrost and Ground-Ice Conditions, Version 2, Boulder, Colorado USA. NSIDC: National Snow and Ice Data Center, https://doi.org/10.7265/skbg-kf16, 2002.

Burn, C. R. and Lewkowicz, A.: Canadian landform examples-17 retrogressive thaw slumps, Canadian Geographer/Le Géographe canadien, 34, 273–276, 1990.

Burn, C. R., Michel, F. A., and Smith, M. W.: Stratigraphic, isotopic, and mineralogical evidence for an early Holocene thaw unconformity at Mayo, Yukon Territory, Canadian Journal of Earth Sciences, 23, 794–803, https://doi.org/10.1139/e86-081, 1986.

Clauset, A., Shalizi, C. R., and Newman, M. E.: Power-law distributions in empirical data, SIAM review, 51, 661–703, 2009.

Dai, C., Jones, M., Howat, I., Liljedahl, A., Lewkowicz, A., and Freymueller, J.: Using ArcticDEM to identify and quantify pan-Arctic retrogressive thaw slump activity, in: EGU General Assembly 2020 Online, 4–8 May 2020 EGU2020-12142, https://doi.org/10.5194/egusphere-egu2020-12142, 2020.

Fritz, T., Rossi, C., Yague-Martinez, N., Rodriguez-Gonzalez, F., Lachaise, M., and Breit, H.: Interferometric processing of TanDEM-X data, in: 2011 IEEE International Geoscience and Remote Sensing Symposium, pp. 2428–2431, https://doi.org/10.1109/IGARSS.2011.6049701, 2011.

Gooseff, M. N., Balser, A., Bowden, W. B., and Jones, J. B.: Effects of hillslope thermokarst in northern Alaska, Eos, Transactions American Geophysical Union, 90, 29–30, 2009.

Grosse, G., Harden, J., Turetsky, M., McGuire, A. D., Camill, P., Tarnocai, C., Frolking, S., Schuur, E. A., Jorgenson, T., Marchenko, S., Romanovsky, V., Wickland, K. P., French, N., Waldrop, M., Bourgeau-Chavez, L., and Striegl, R. G.: Vulnerability of high-latitude soil organic carbon in North America to disturbance, Journal of Geophysical Research: Biogeosciences, https://doi.org/10.1029/2010JG001507, 2011.

Jones, M. K. W., Pollard, W. H., and Jones, B. M.: Rapid initialization of retrogressive thaw slumps in the Canadian high Arctic and their response to climate and terrain factors, Environmental Research Letters, 14, 055 006, 2019.

Kang-tsung, C. and Bor-wen, T.: The Effect of DEM Resolution on Slope and Aspect Mapping, Cartography and Geographic Information Systems, 18, 69–77, https://doi.org/10.1559/152304091783805626, 1991.

Kaplan, G. and Avdan, U.: Object-based water body extraction model using Sentinel-2 satellite imagery, European Journal of Remote Sensing, https://doi.org/10.1080/22797254.2017.1297540, 2017.

Kaufman, D., Ager, T., Anderson, N., Anderson, P., Andrews, J., Bartlein, P., Brubaker, L., Coats, L., Cwynar, L., Duvall, M., Dyke, A., Edwards, M., Eisner, W., Gajewski, K., Geirsdóttir, A., Hu, F., Jennings, A., Kaplan, M., Kerwin, M., Lozhkin, A., MacDonald, G., Miller, G., Mock, C., Oswald, W., Otto-Bliesner, B., Porinchu, D., Rühland, K., Smol, J., Steig, E., and Wolfe, B.: Holocene thermal maximum in the western Arctic (0–180W), Quaternary Science Reviews, 23, 529 – 560, https://doi.org/10.1016/j.quascirev.2003.09.007, 2004.

Klar, A., Aharonov, E., Kalderon-Asael, B., and Katz, O.: Analytical and observational relations between landslide volume and surface area, Journal of Geophysical Research: Earth Surface, 116, 2011.

Kokelj, S. V. and Jorgenson, M. T.: Advances in thermokarst research, Permafrost and Periglacial Processes, 24, 108–119, https://doi.org/10.1002/ppp.1779, 2013.

Kokelj, S. V., Lantz, T. C., Kanigan, J., Smith, S. L., and Coutts, R.: Origin and polycyclic behaviour of tundra thaw slumps, Mackenzie Delta region, Northwest Territories, Canada, Permafrost and Periglacial Processes, 20, 173–184, https://doi.org/10.1002/ppp.642, 2009.

Kokelj, S. V., Lantz, T. C., Tunnicliffe, J., Segal, R., and Lacelle, D.: Climate-driven thaw of permafrost preserved glacial landscapes, northwestern Canada, Geology, 45, 371–374, https://doi.org/10.1130/G38626.1, 2017.

Kokelj, S. V., Kokoszka, J., van der Sluijs, J., Rudy, A. C. A., Tunnicliffe, J., Shakil, S., Tank, S. E., and Zolkos, S.: Thaw-driven mass wasting couples slopes with downstream systems, and effects propagate through Arctic drainage networks, The Cryosphere, 15, 3059–3081, https://doi.org/10.5194/tc-15-3059-2021, 2021.

Krieger, G., Moreira, A., Fiedler, H., Hajnsek, I., Werner, M., Younis, M., and Zink, M.: TanDEM-X: A satellite formation for high-resolution SAR interferometry, in: IEEE Transactions on Geoscience and Remote Sensing, vol. 45, pp. 3317–3340, https://doi.org/10.1109/TGRS.2007.900693, 2007.

Lacelle, D., Bjornson, J., Lauriol, B., Clark, I., and Troutet, Y.: Segregated-intrusive ice of subglacial meltwater origin in retrogressive thaw flow headwalls, Richardson Mountains, NWT, Canada, Quaternary Science Reviews, 23, 681 – 696, https://doi.org/10.1016/j.quascirev.2003.09.005, 2004.

Lacelle, D., Bjornson, J., and Lauriol, B.: Climatic and geomorphic factors affecting contemporary (1950-2004) activity of retrogressive thaw slumps on the Aklavik plateau, Richardson mountains, NWT, Canada, Permafrost and Periglacial Processes, 21, 1–15, https://doi.org/10.1002/ppp.666, 2010.

Lacelle, D., Brooker, A., Fraser, R. H., and Kokelj, S. V.: Distribution and growth of thaw slumps in the Richardson Mountains-Peel Plateau region, northwestern Canada, Geomorphology, 235, 40–51, https://doi.org/10.1016/j.geomorph.2015.01.024, 2015.

Lantuit, H. and Pollard, W. H.: Fifty years of coastal erosion and retrogressive thaw slump activity on Herschel Island, southern Beaufort Sea, Yukon Territory, Canada, Geomorphology, 95, 84–102, https://doi.org/10.1016/j.geomorph.2006.07.040, 2008.

Lantuit, H., Pollard, W. H., Couture, N., Fritz, M., Schirrmeister, L., Meyer, H., and Hubberten, H.-W.: Modern and Late Holocene Retrogressive Thaw Slump Activity on the Yukon Coastal Plain and Herschel Island, Yukon Territory, Canada, Permafrost and Periglacial Processes, 23, 39–51, https://doi.org/10.1002/ppp.1731, 2012.

Lantz, T. C. and Kokelj, S. V.: Increasing rates of retrogressive thaw slump activity in the Mackenzie Delta region, N.W.T., Canada, Geophysical Research Letters, 35, https://doi.org/10.1029/2007GL032433, 2008.

Larsen, Montgomery, and Korup: Landslide erosion controlled by hillslope material, Nature Geoscience, 3, 247–251, 2010.

Leinss, S. and Bernhard, P.: TanDEM-X: Deriving InSAR height changes and velocity dynamics of great aletsch glacier, IEEE Journal of Selected Topics in Applied Earth Observations and Remote Sensing, 14, 4798–4815, 2021.

Lewkowicz, A. G.: Headwall retreat of ground-ice slumps, Banks Island, Northwest Territories, Canadian Journal of Earth Sciences, https://doi.org/10.1139/e87-105, 1987a.

Lewkowicz, A. G.: Nature and Importance of Thermokarst Processes, Sand Hills Moraine, Banks Island, Canada, Geografiska Annaler: Series A, Physical Geography, 69, 321–327, https://doi.org/10.1080/04353676.1987.11880218, 1987b.

Lewkowicz, A. G. and Way, R. G.: Extremes of summer climate trigger thousands of thermokarst landslides in a High Arctic environment, Nature Communications, https://doi.org/10.1038/s41467-019-09314-7, 2019.

Malamud, B. D., Turcotte, D. L., Guzzetti, F., and Reichenbach, P.: Landslide inventories and their statistical properties, Earth Surface Processes and Landforms, 29, 687–711, https://doi.org/10.1002/esp.1064, 2004.

Markovsky, I. and Van Huffel, S.: Overview of total least-squares methods, Signal Processing, 87, 2283 – 2302, https://doi.org/10.1016/j.sigpro.2007.04.004, special Section: Total Least Squares and Errors-in-Variables Modeling, 2007.

Martone, M., Bräutigam, B., Rizzoli, P., Gonzalez, C., Bachmann, M., and Krieger, G.: Coherence evaluation of TanDEM-X interferometric data, ISPRS Journal of Photogrammetry and Remote Sensing, 73, 21–29, https://doi.org/https://doi.org/10.1016/j.isprsjprs.2012.06.006, innovative Applications of SAR Interferometry from modern Satellite Sensors, 2012.

McFeeters, S. K.: The use of the Normalized Difference Water Index (NDWI) in the delineation of open water features, International Journal of Remote Sensing, https://doi.org/10.1080/01431169608948714, 1996.

Millan, R., Dehecq, A., Trouvé, E., Gourmelen, N., and Berthier, E.: Elevation changes and X-band ice and snow penetration inferred from TanDEM-X data of the Mont-Blanc area, in: 2015 8th International Workshop on the Analysis of Multitemporal Remote Sensing Images (Multi-Temp), pp. 1–4, https://doi.org/10.1109/Multi-Temp.2015.7245753, 2015.

Nesterova, N., Khomutov, A., Kalyukina, A., and Leibman, M.: The specificity of thermal denudation feature distribution on Yamal and Gydan peninsulas Russia, in: EGU General Assembly 2020 Online, 4–8 May 2020, EGU2020-746, https://doi.org/10.5194/egusphere-egu2020-746, 2019.

Nicu, I. C., Lombardo, L., and Rubensdotter, L.: Preliminary assessment of thaw slump hazard to Arctic cultural heritage in Nordenskiöld Land, Svalbard, Landslides, pp. 1–13, 2021.

Nitze, I., Grosse, G., Jones, B. M., Arp, C. D., Ulrich, M., Fedorov, A., and Veremeeva, A.: Landsat-based trend analysis of lake dynamics across Northern Permafrost Regions, Remote Sensing, 9, https://doi.org/10.3390/rs9070640, 2017.

Nitze, I., Grosse, G., Jones, B., Romanovsky, V., and Boike, J.: Remote sensing quantifies widespread abundance of permafrost region disturbances across the Arctic and Subarctic, Nature communications, 9, 1–11, 2018.

Obu, J.: How Much of the Earth's Surface is Underlain by Permafrost?, Journal of Geophysical Research: Earth Surface, 126, e2021JF006 123, https://doi.org/https://doi.org/10.1029/2021JF006123, e2021JF006123 2021JF006123, 2021.

Ohtani, K.: Bootstrapping R2 and adjusted R2 in regression analysis, Economic Modelling, 17, 473–483, https://doi.org/10.1016/S0264-9993(99)00034-6, 2000.

Parker, R., Hancox, G., Petley, D., Massey, C., Densmore, A., and Rosser, N.: Spatial distributions of earthquake-induced landslides and hillslope preconditioning in northwest South Island, New Zealand., Earth surface dynamics., 3, 501–525, 2015.

Planet-Team: Planet Application Program Interface: In Space for Life on Earth, https://api.planet.com, 2018.

Ramage, J. L., Irrgang, A. M., Herzschuh, U., Morgenstern, A., Couture, N., and Lantuit, H.: Terrain Controls on the Occurrence of Coastal Retrogressive Thaw Slumps along the Yukon Coast, Canada, Journal of Geophysical Research: Earth Surface, https://doi.org/10.1002/2017JF004231, 2017.

Rudy, A. C., Lamoureux, S. F., Kokelj, S. V., Smith, I. R., and England, J. H.: Accelerating Thermokarst Transforms Ice-Cored Terrain Triggering a Downstream Cascade to the Ocean, Geophysical Research Letters, https://doi.org/10.1002/2017GL074912, 2017.

Schuur, E. A. G., McGuire, A. D., Schädel, C., Grosse, G., Harden, J. W., Hayes, D. J., Hugelius, G., Koven, C. D., Kuhry, P., Lawrence, D. M., Natali, S. M., Olefeldt, D., Romanovsky, V. E., Schaefer, K., Turetsky, M. R., Treat, C. C., and Vonk, J. E.: Climate change and the permafrost carbon feedback, Nature, 520, https://doi.org/10.1038/nature14338, 2015.

Segal, R. A., Lantz, T. C., and Kokelj, S. V.: Acceleration of thaw slump activity in glaciated landscapes of the Western Canadian Arctic, Environmental Research Letters, 11, 034 025, https://doi.org/10.1088/1748-9326/11/3/034025, 2016.

Swanson, D. K. and Nolan, M.: Growth of retrogressive thaw slumps in the Noatak Valley, Alaska, 2010-2016, measured by airborne photogrammetry, Remote Sensing, https://doi.org/10.3390/rs10070983, 2018.

Tanyaş, H., Allstadt, K. E., and van Westen, C. J.: An updated method for estimating landslide-event magnitude, Earth Surface Processes and Landforms, 43, 1836–1847, https://doi.org/10.1002/esp.4359, 2018.

Tebbens, S. F.: Landslide Scaling: A Review, Earth and Space Science, 7, e2019EA000 662, https://doi.org/10.1029/2019EA000662, e2019EA000662 2019EA000662, 2020.

Turcotte, D. L.: Self-organized criticality, Reports on progress in physics, 62, 1377, 1999.

Turetsky, M. R., Abbott, B. W., Jones, M. C., Anthony, K. W., Olefeldt, D., Schuur, E. A., Grosse, G., Kuhry, P., Hugelius, G., Koven, C., et al.: Carbon release through abrupt permafrost thaw, Nature Geoscience, 13, 138–143, 2020.

Van der Sluijs, J., Kokelj, S. V., Fraser, R. H., Tunnicliffe, J., and Lacelle, D.: Permafrost terrain dynamics and infrastructure impacts revealed by UAV photogrammetry and thermal imaging, Remote Sensing, 10, 1734, 2018.

Wang, B., Paudel, B., and Li, H.: Retrogression characteristics of landslides in fine-grained permafrost soils, Mackenzie Valley, Canada, Landslides, 6, 121–127, 2009.

Wang, B., Paudel, B., and Li, H.: Behaviour of retrogressive thaw slumps in northern Canada—three-year monitoring results from 18 sites, Landslides, 13, 1–8, 2016.

Werner, C., Wegmueller, U., Strozzi, T., and Wiesmann, A.: GAMMA SAR and interferometric processing software, in: European Space Agency, (Special Publication) ESA SP, 461, pp. 211–219, 2000.

Zwieback, S., Kokelj, S., Günther, F., Boike, J., Grosse, G., and Hajnsek, I.: Sub-seasonal thaw slump mass wasting is not consistently energy limited at the landscape scale, Cryosphere, https://doi.org/10.5194/tc-12-549-2018, 2018.

Zwieback, S., Boike, J., Marsh, P., and Berg, A.: Debris cover on thaw slumps and its insulative role in a warming climate, Earth Surface Processes and Landforms, 45, 2631–2646, https://doi.org/10.1002/esp.4919, 2020.

Supplement to Assessing volumetric change distributions and scaling relations of thaw slumps across the Arctic

Philipp Bernhard[1], Simon Zwieback[2], Nora Bergner[1], and Irena Hajnsek[1,3]

[1]Institute of Environmental Engineering, ETH Zurich, 8093 Zurich, Switzerland ETH Zürich
[2]Geophysical Institute, University of Alaska Fairbanks, Fairbanks, AK 99775 USA
[3]Microwaves and Radar Institute, German Aerospace Center (DLR) e.V., 82234 Wessling, Germany

Correspondence: Philipp Bernhard (bernhard@ifu.baug.ethz.ch)

1 Propbility density function of area and volumetric change rates

To compute the rollover, cutoff, exponetial decay coefficients we fitted a a three-parameter inverse Gamma function defined by:

$$pdf(X_{RTS}|\rho,a,s) = \frac{1}{a\Gamma(\rho)}\left(\frac{1}{X_{RTS}-s}\right)^{\rho+1}\exp\left(-\frac{a}{X_{RTS}-s}\right) \quad (1)$$

where X_{RTS} is either the yearly area or volume change and $\Gamma(\rho)$ is the gamma function of ρ. The determined values of the fitting parameters as well as the rollover, cutoff and exponential decay coefficients can be seen in Table S1 and S2.

Table S 1. Rollover Cutoff and Exponential decay for yearly area change rate.

Area	Rollover $[10^2 \mathrm{m}^2 \mathrm{yr}^{-1}]$	Cutoff $[10^3 \mathrm{m}^2 \mathrm{yr}^{-1}]$	Exp.decay	ρ	a $[10^3]$	s $[10^3]$
Peel	4.96 ± 0.48	1.98 ± 0.94	2.4 ± 0.4	1.45	1.47	-0.11
Banks	10.84 ± 0.66	3.95 ± 2.10	3.0 ± 0.5	1.76	3.60	-0.21
Ellesmere	11.46 ± 0.98	5.41 ± 2.74	3.2 ± 0.9	1.49	3.10	-0.10
Tuktuyaktuk	2.42 ± 0.43	1.31 ± 0.24	3.6 ± 0.8	1.82	0.76	-0.03
Noatak	4.89 ± 1.79	1.23 ± 0.21	2.8 ± 0.6	12.9	27.62	-1.38
Chukotka	3.36 ± 1.50	1.13 ± 0.15	3.2 ± 0.5	29.59	100.76	-2.82
Taymyr	4.02 ± 0.28	1.15 ± 0.24	3.0 ± 0.4	0.85	0.34	-0.19
Yamal/Gydan	3.92 ± 0.73	1.36 ± 0.20	3.7 ± 1.2	4.26	4.34	-0.41

Table S 2. Rollover Cutoff and Exponential decay for yearly volumetric change rate.

Area	Rollover $[10^2 \mathrm{m}^3 \mathrm{yr}^{-1}]$	Cutoff $[10^3 \mathrm{m}^3 \mathrm{yr}^{-1}]$	Exp.decay	ρ	a $[10^3]$	s $[10^3]$
Peel	15.21 ± 1.86	3.31 ± 1.60	1.9 ± 0.1	0.97	3.71	-0.37
Banks	16.57 ± 1.14	5.34 ± 2.96	2.0 ± 0.2	0.95	3.33	-0.05
Ellesmere	29.83 ± 4.34	3.97 ± 2.73	1.9 ± 0.2	1.28	7.17	-0.32
Tuktuyaktuk	7.28 ± 0.67	1.35 ± 0.84	2.3 ± 0.2	2.15	2.89	-0.20
Noatak	5.83 ± 3.36	1.58 ± 0.45	2.1 ± 0.3	0.73	0.63	-0.14
Chukotka	10.42 ± 4.70	2.19 ± 0.90	2.6 ± 0.5	7.22	32.29	-2.55
Taymyr	9.63 ± 1.71	2.06 ± 1.40	2.3 ± 0.5	0.97	1.32	0.26
Yamal/Gydan	10.23 ± 2.93	2.41 ± 0.88	2.8 ± 0.6	4.25	12.54	-1.23

2 Additional Figures

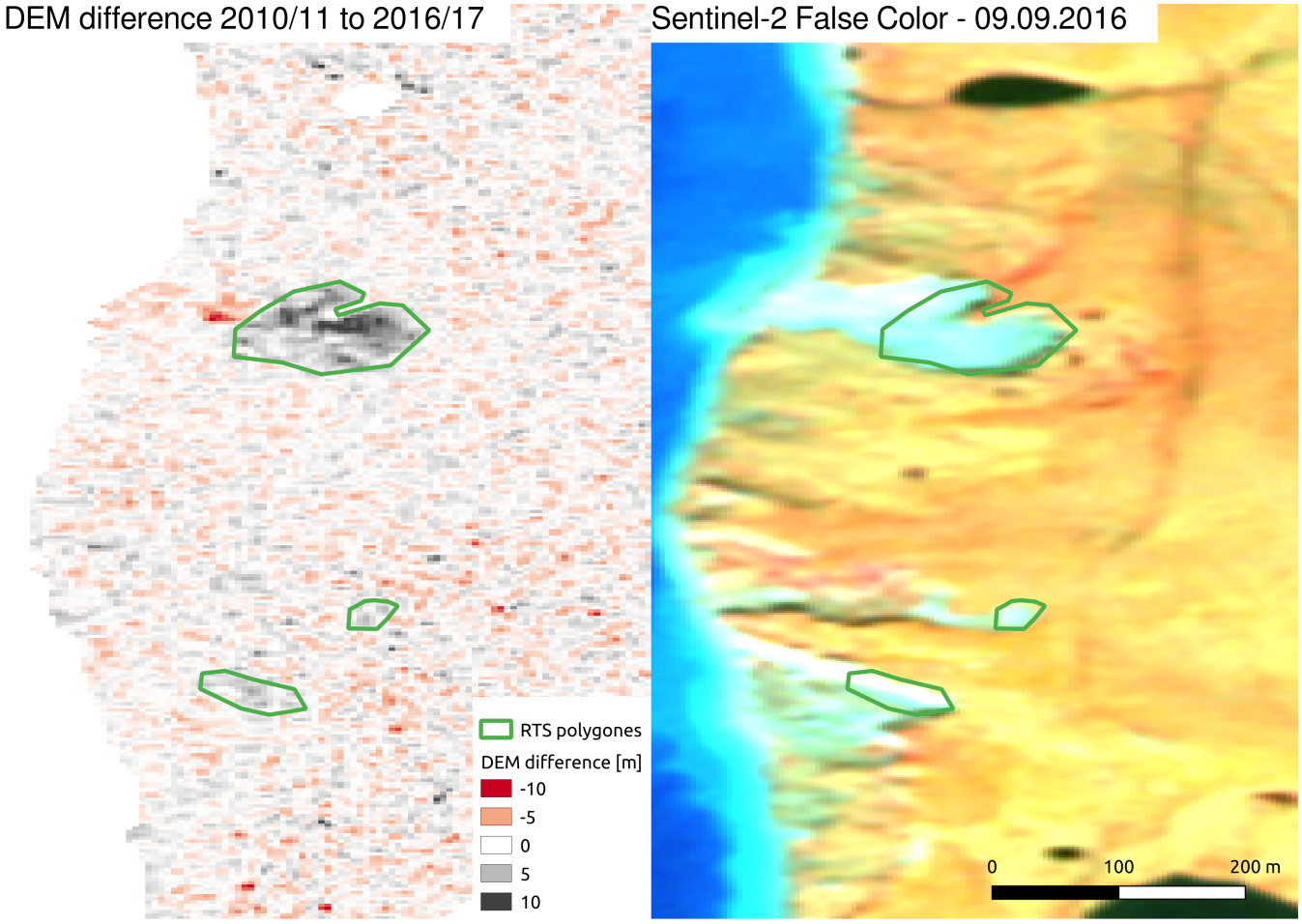

Figure S 1. Example of RTS polygones in the Chukotka study region located at N65.93 W-178.82. Left: DEM difference image between winter 2010/11 and 2016/17. Right: False color Sentinel-2 image taken on ~~the~~ 09.09.2016.

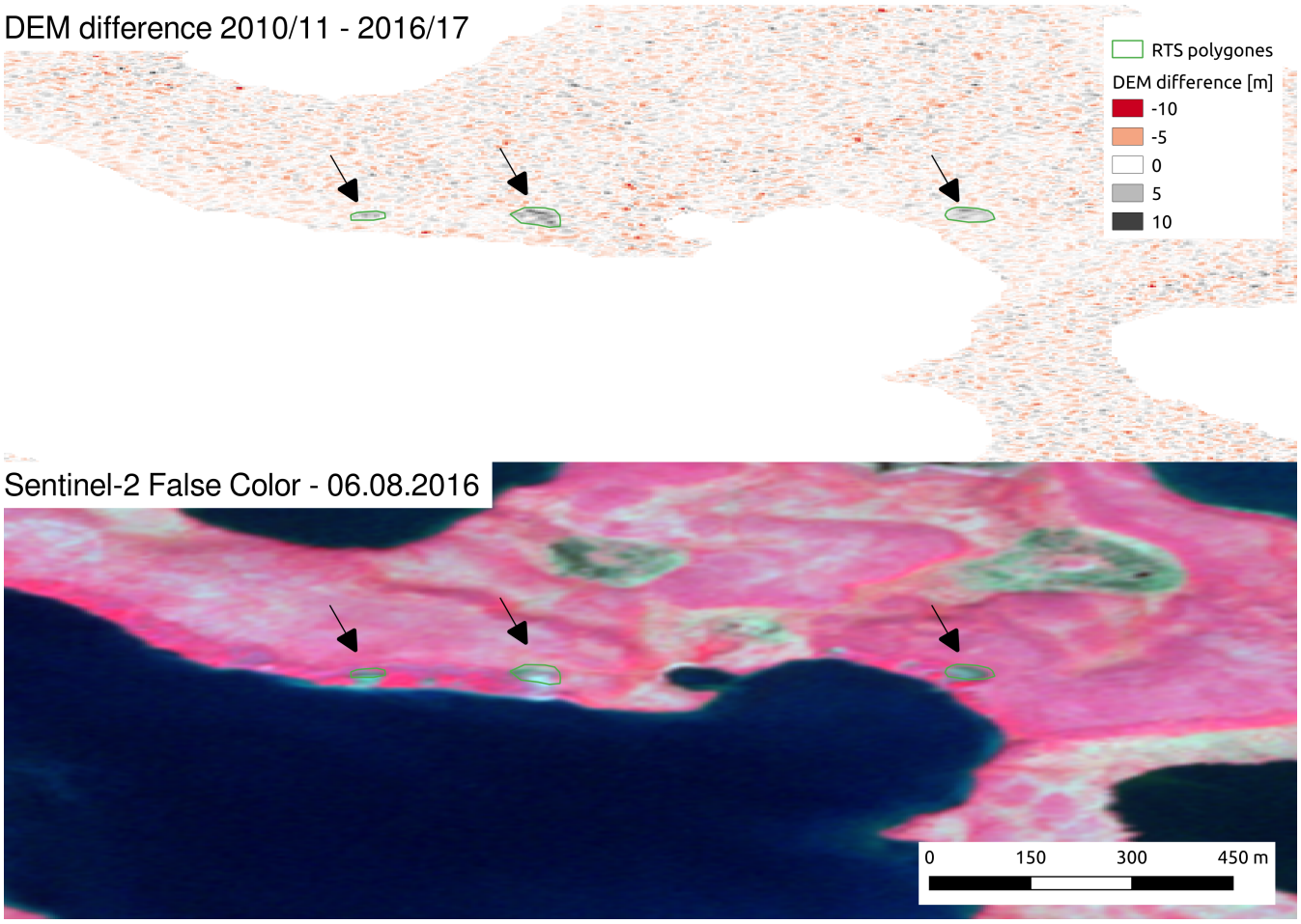

Figure S 2. Example of RTS polygones in the Tuktoyaktuk study region located at N69.08 W-134.02. The black arrows indicate the RTS lcoations Left: DEM difference image between winter 2010/11 and 2016/17. Right: False color Sentinel-2 image taken on ~~the~~ 06.08.2016.

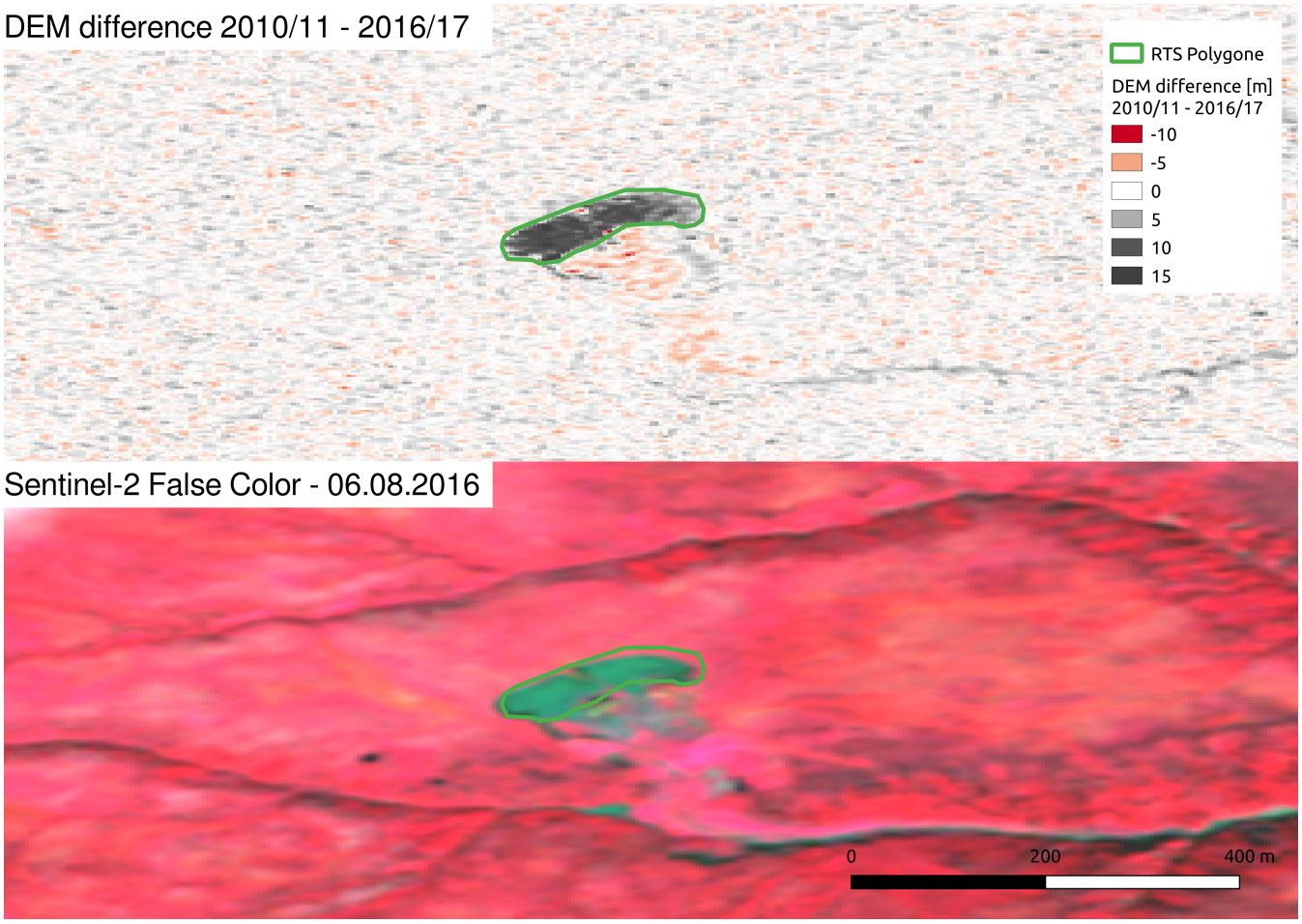

Figure S 3. Example of RTS polygones in the Peel study region located at N67.26 W-135.27. Left: DEM difference image between winter 2010/11 and 2016/17. Right: False color Sentinel-2 image taken on ~~the~~ 06.08.2016.

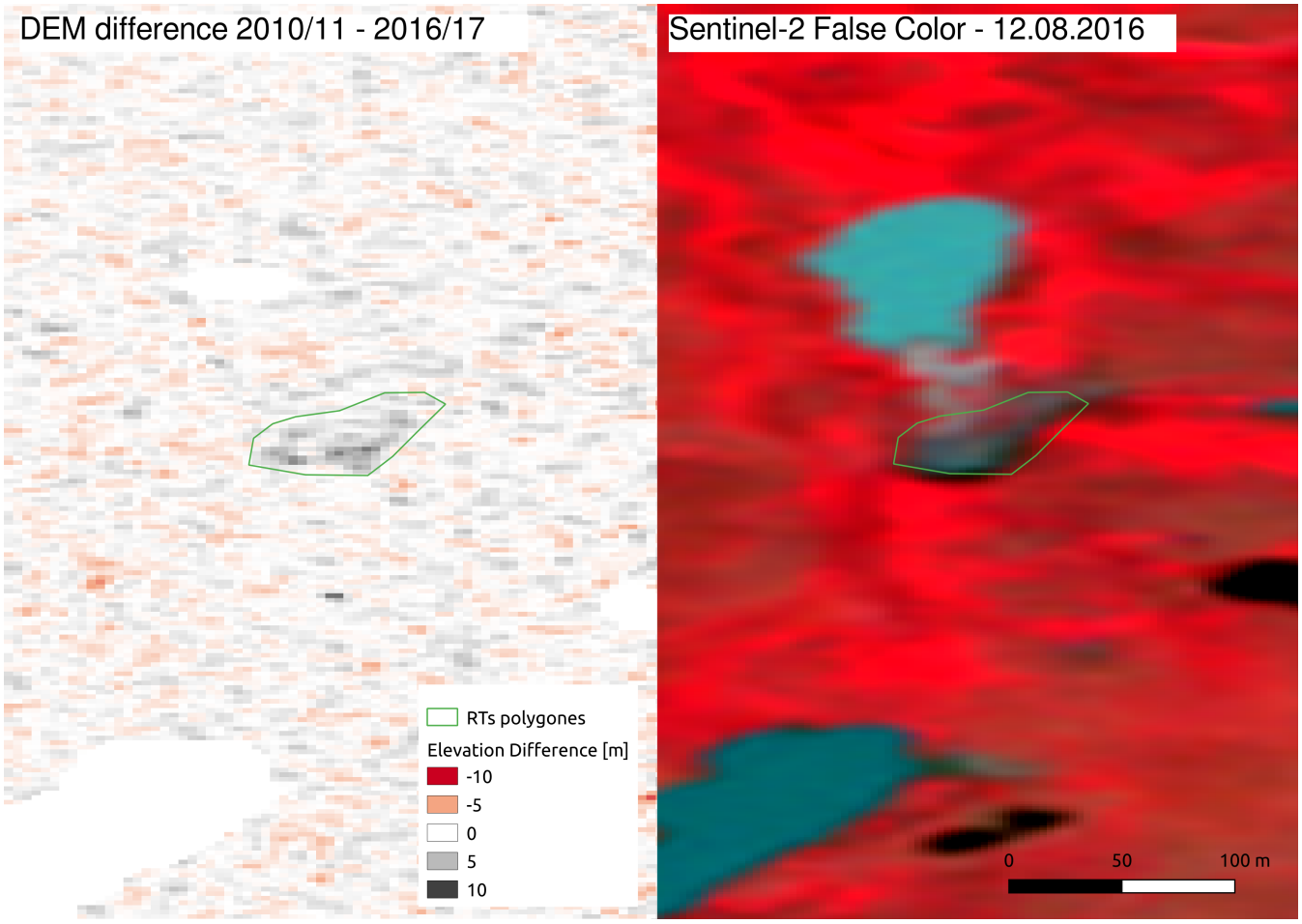

Figure S 4. Example of RTS polygones in the Yamal study region located at N71.09 W70.40 . Left: DEM difference image between winter 2010/11 and 2016/17. Right: Fasle color Sentinel-2 image taken on ~~the~~ 12.08.2016.

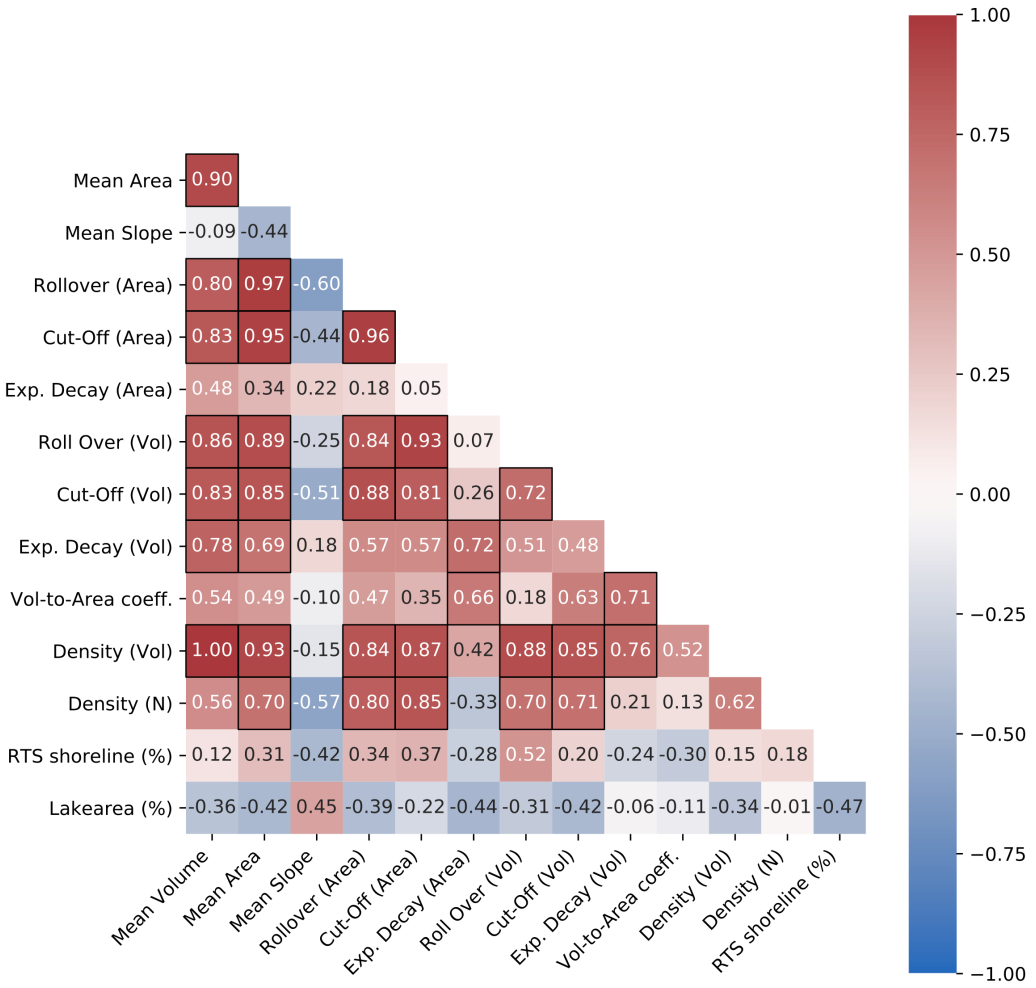

Figure S 5. Correlation coefficients between all computed quantities of all areas. ~~A value~~ below -0.64 and above 0.64 are statistically significant (t-Test with a p-value < 0.05).

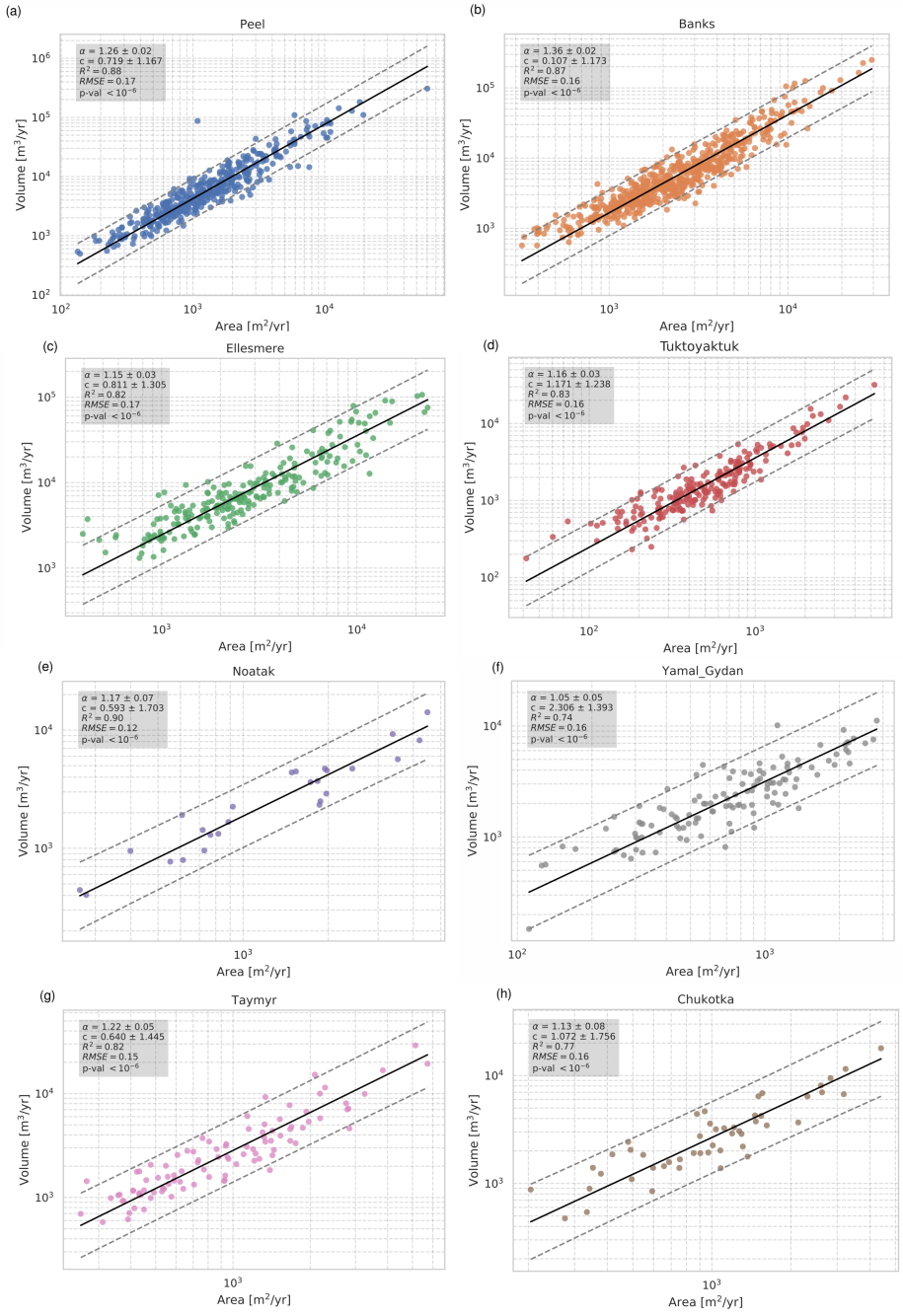

Figure S 6. Area to Volume scaling for each study area.

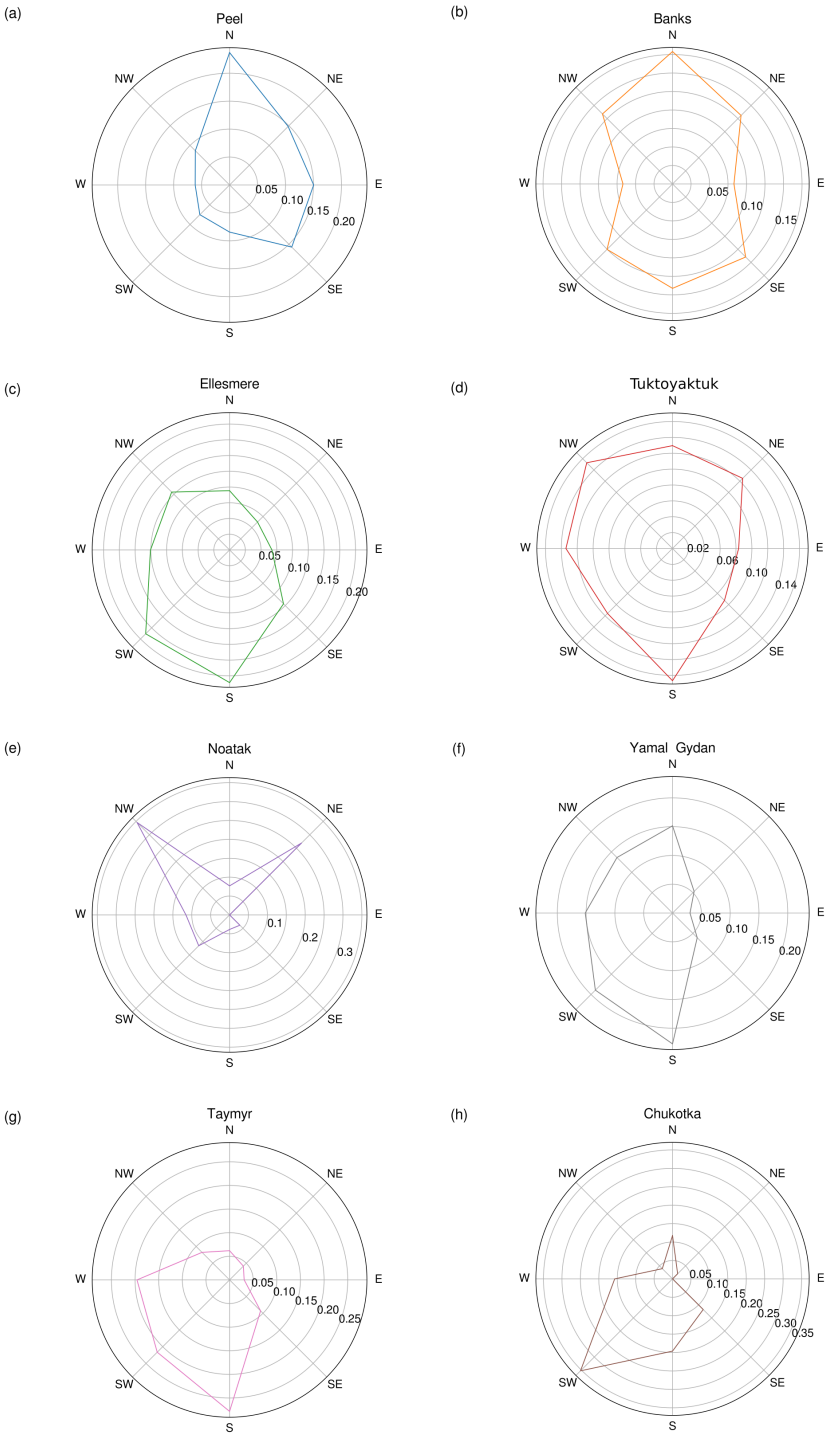

Figure S 7. Aspect distribution of all study areas.